STARS

2014

Multifunctional, Multimaterial Particle Fabrication Via an In-Fiber Fluid Instability

Joshua Kaufman

University of Central Florida

Showcase of Text, Archives, Research & Scholarship

MULTIFUNCTIONAL, MULTIMATERIAL PARTICLE FABRICATION VIA AN IN-FIBER FLUID INSTABILITY

by

JOSHUA KAUFMAN
B.S. in Electrical and Computer Engineering; Purdue University, West Lafayette, IN; spring 2008

A dissertation submitted in partial fulfillment of the requirements
for the degree of Doctor of Philosophy
in CREOL, the College of Optics & Photonics
at the University of Central Florida
Orlando, Florida

Summer Term
2014

Major Professor: Ayman Abouraddy

ABSTRACT

Spherical micro- and nano-particles have found widespread use in many various applications from paint to cosmetics to medicine. Due to the multiplicity of desired particle material(s), structure, size range, and functionality, many approaches exist for generating such particles. Bottom-up methods such as chemical synthesis have a high yield and work with a wide range of materials; however, these processes typically lead to large polydispersity and cannot produce structured particles. Top-down approaches such as microfluidics overcome the polydispersity issue and may produce a few different structures in particles, but at lower rates and only at the micro-scale. A method that can efficiently produce uniformly-sized, structured particles out of a variety of materials and at both the micro- and nano-scales does not yet exist.

Over the past few years, I have developed an in-fiber particle fabrication method that relies on a surface tension-driven fluid instability, the Plateau-Rayleigh capillary instability (PRI). Thermal treatment of a multimaterial core/cladding fiber induces the PRI, causing the initially intact core to break up into a periodic array of uniformly-sized spherical particles. During this time, I have demonstrated that this method can produce particles from both polymers and glasses, in a multiplicity of structures, and from diameters of over 1 mm down to 20 nm. Furthermore, by using a stack-and-draw method, a high density of cores may be incorporated into a single fiber, making the in-fiber PRI approach a highly scalable process. Finally, I have shown that it is possible to add dopants to the particles to give them functionality. By structuring the particles, it is thus possible to fabricate multi-functional particles whose functionalities may be allocated arbitrarily throughout the volume of the particles.

Dedicated to all my friends and family

ACKNOWLEDGMENTS

I would like to deeply thank my Ph.D. advisor, Dr. Ayman Abouraddy. He has guided me throughout my time at CREOL and has always made himself available to me to provide me with new ideas. He has also pushed me to accomplish more than I thought I could.

I would also like to thank my committee members: professors Christodoulides, Schoenfeld, and Seal. Professor Yoel Fink and Professor Steven Johnson at MIT have also been very helpful in collaborating with me on projects and have provided great help and constructive criticism. My other collaborators Rick Ottman and Professor Ratna Chakrabarti have also been of great help and have done great work in our combined efforts.

All of the employees at the Materials Characterization Facility have also been of great help in all of my work on SEM, TEM, FIB, Microtome, and Raman microscopy. Special thanks to Kirk, Mikhail, and Karen.

Lastly, many thanks to everyone at CREOL, especially my groupmates: Catherine Li, Felix Tan, Soroush Shabahang, Guangming Tao, and Hooman Banaei.

TABLE OF CONTENTS

LIST OF FIGURES

Figure 8. Polymer-core/glass-shell spherical particle fabrication. a, Schematic of the fiber structure (P, G as in Figs 1, 2). b, c, SEM images of fiber cross-sections. d, SEM image of the glass-shell outer surface, showing the modulation characteristic of the PRI. e, SEM image of the structure in d after sectioning off half of the glass shell using a focused ion beam (FEI 200 THP; current ,10–100 pA), revealing the correlated modulations on the two interfaces (inner polymer/glass and outer glass/polymer interfaces), and resulting ultimately in two concentric spherical surfaces as shown in g and h. f, Three snapshots from a three-dimensional simulation of the Stokes equations using a representative fiber structure, illustrating

the full breakup process. Time progresses from top to bottom. Scale bar, 50 mm. Dark green, polymer core; light green, glass shell; the outer polymer scaffold cladding is made transparent for clarity. g, Top and h, front (tilted) SEM views of four differently sized core–shell particles (outer diameters 34 mm, 7 mm, 1.2 mm and 650 nm, respectively). Scale bars in the corresponding top and front views are the same length. 16

INTRODUCTION

From drug delivery[1,2] to chemical and biological catalysis[3] and cosmetics[4], the need for efficient fabrication pathways for particles over a wide range of sizes, from a variety of materials, and in many different structures has been well established[5]. Bottom-up approaches to particle synthesis—through nucleation, chemical reactions or self-assembly[6,7]—yield nanometer-scale particles from a variety of materials. The particles produced using such approaches are typically characterized by a large dispersion in the size and shape distribution, and are hampered by coalescence and agglomeration during particle growth. Producing complex multimaterial structures or mono-disperse micro-sized particles is technologically challenging in bottom-up synthesis approaches. On the other hand, top-down approaches[8]—such as microfluidics[9,10], lithography[11,12] and imprint lithography[13]—typically yield larger, mono-disperse particles, but are each suited to a specific material and size range determined by the underlying kinetics of the process. Lithography and imprint lithography produce nanoparticles at low rates, because the produced volume scales with particle size in two dimensional processes. Furthermore, fabricating structured spherical particles requires non-trivial modifications to these approaches, which ultimately impose constraints on the number of geometric features and types of material combined in a particle. My new, scalable process uses a fluid instability occurring within a multimaterial fiber to produce a necklace of spherical particles inside the fiber, with complex geometries combining predetermined ratios of multiple materials, made with the same ease as producing single-material particles.

Polymeric particles in particular have found many uses in biology and medicine. Medical applications in diagnostics[14], imaging[15,16], and drug delivery[17] typically make use of micro- and nanoparticles in two distinct modes: The surfaces may serve as loci for chemical or biological interactions through surface functionalization[18], or, alternatively, the volume may be used to carry cargo[19,20] for drug delivery and multidimensional imaging modalities[21]. Polymeric nanoparticles in particular are steadily gaining importance in medicine because of their long half-life in the blood stream[22,23] and the versatility by which their composition, size, shape, and physicochemical properties[24] may be tuned via a variety of processing approaches. Recent medical achievements based on the use of polymer particles in specific applications include the targeted delivery of drugs and toxins using surface-conjugated biodegradable polymer particles[25,26], treatment of antibiotic-resistant bacterial infections[27,28], and induction of regulatory T cells for treatment of multiple sclerosis[29].

My work has been dedicated to harnessing the inherent scalability of fiber production[30] and an in-fiber Plateau–Rayleigh capillary instability[31] (PRI) for the fabrication of uniformly sized, structured spherical particles. This process can yield particles spanning an exceptionally wide range of sizes: from 2mmdown to 20 nm. Thermal processing of a multimaterial fiber[32] controllably induces the PRI[33], resulting in a well ordered, oriented emulsion[34] in three dimensions. The fiber core and cladding correspond to the dispersed and continuous phases, respectively, and are both frozen in situ on cooling, after which the particles are released when needed. By arranging a variety of structures and materials in a macroscopic scaled-up model of the fiber, I produce composite, structured, spherical particles, such as core–shell particles, two-compartment 'Janus' particles[35], and multi-sectioned 'beach ball' particles. Moreover, producing

fibers with a high density of cores allows for an unprecedented level of parallelization: in principle, 10^8 50-nm cores or 10^3 10-µm cores embedded in meters-long, 1-mm-diameter fiber, which can be induced to break up simultaneously throughout its length, into uniformly sized, structured spheres.

The two classes of particle materials I have investigated are low-temperature chalcogenide glasses and polymers. First, I will discuss the work concentrating on chalcogenide glass particles. This will outline the mechanics of the particle formation process, the scale invariance of the PRI, the ability to scale the process to increase production rates, and how it is possible to generate particles with complex structures. The second section of this manuscript will deal with polymer particle fabrication and its possible relevance to research in biology and medicine.

CHAPTER 1 IN-FIBER GLASS PARTICLE FABRICATION

1.1   Fiber Fabrication and Particle Generation

Figure 1 outlines my approach to particle generation. The procedure starts with the preparation of a macroscopic scale model, called a 'preform', whose core is assembled from the intended particle constituent materials encased in a scaffold. The preform is then thermally drawn into an extended fiber[30,32], until the core diameter approaches the required particle size (Fig. 1a). Figure 1b shows an example of a fiber cross-section, comprising an amorphous, semiconducting chalcogenide glass core (As_2Se_3) encased in a polymer cladding (polyethersulphone, PES). The multimaterial preform during the draw is analogous to concentric, co-flowing, focused jets[31]. To ensure the integrity of the core, the preform is thermally drawn in a high-viscosity regime ($>10^6$ Pa s), and the fiber emerging from the heating zone is cooled quickly to arrest the development of any axial instability. This drawing process produces axially stable cores[36] with diameters from >1mm to <3 nm, which sets the upper and lower limits on the potential particle sizes.

Thermal treatment of this fiber induces the PRI[31,33], resulting in the breakup of the continuous core into an orderly arrangement of spherical particles held immobile in the cladding. The full dynamics of the breakup process are captured by applying a temperature gradient along the axis of a fiber section (Fig. 1c). At the low-temperature end, the highly viscous core remains intact. As temperature increases (and viscosity decreases), surface tension dominates and a sinusoidal modulation develops at the core–cladding interface, leading ultimately to the breakup of the core into a string of spherical particles. It is also possible to heat the fiber uniformly so that the entire length undergoes breakup. In contrast to the rapid cooling after fiber drawing, the stationary fiber is maintained at elevated temperature for an extended period of time, allowing the core to break up into uniformly sized droplets which are frozen in situ on cooling. The particles may be subsequently released when needed by dissolving the scaffold. My

approach is a thermally driven emulsification of dispersed phase particles (derived from the core) suspended in an immiscible continuous-phase fluid (the scaffold cladding)[37]. The core may be considered a pre-filled fluidic channel[9], filled during the construction of the centimeter-scale preform in the solid state, which is reduced to a high-viscosity fluid during the fiber draw and subsequent thermal processing.

This approach to particle fabrication by multimaterial in-fiber emulsification has several favorable features. First, it can produce uniformly sized spherical particles over an extremely wide size span. This may be appreciated by modeling the fiber core at elevated temperature as a viscous fluid thread surrounded by an infinitely extended viscous immiscible fluid, and making use of the classical Tomotika linear stability theory[38] to calculate the instability growth time τ for potential instability wavelengths λ. The fastest-growing λ (corresponding to the smallest τ) at which the breakup is favored to occur for different values of temperature T and core diameter D may be obtained (Fig. 1d). In general, τ is linearly proportional to D and inversely dependent on T. In this model, a core will break up, at any fixed T, after heating for a sufficiently long time. I have drawn fibers with core diameters ranging from ~2mm down to 20nm and used them to produce particles with perfectly spherical and exquisitely smooth-surfaced external morphology over the entire size span (Fig. 1e, f), confirmed by scanning electron microscope (SEM) imaging after dissolving the polymer cladding using dimethylacetamide[39]. This size span corresponds to five orders of magnitude in linear dimension—fifteen in volume, from ~ 8mm^3 to ~ 8,000 nm^3.
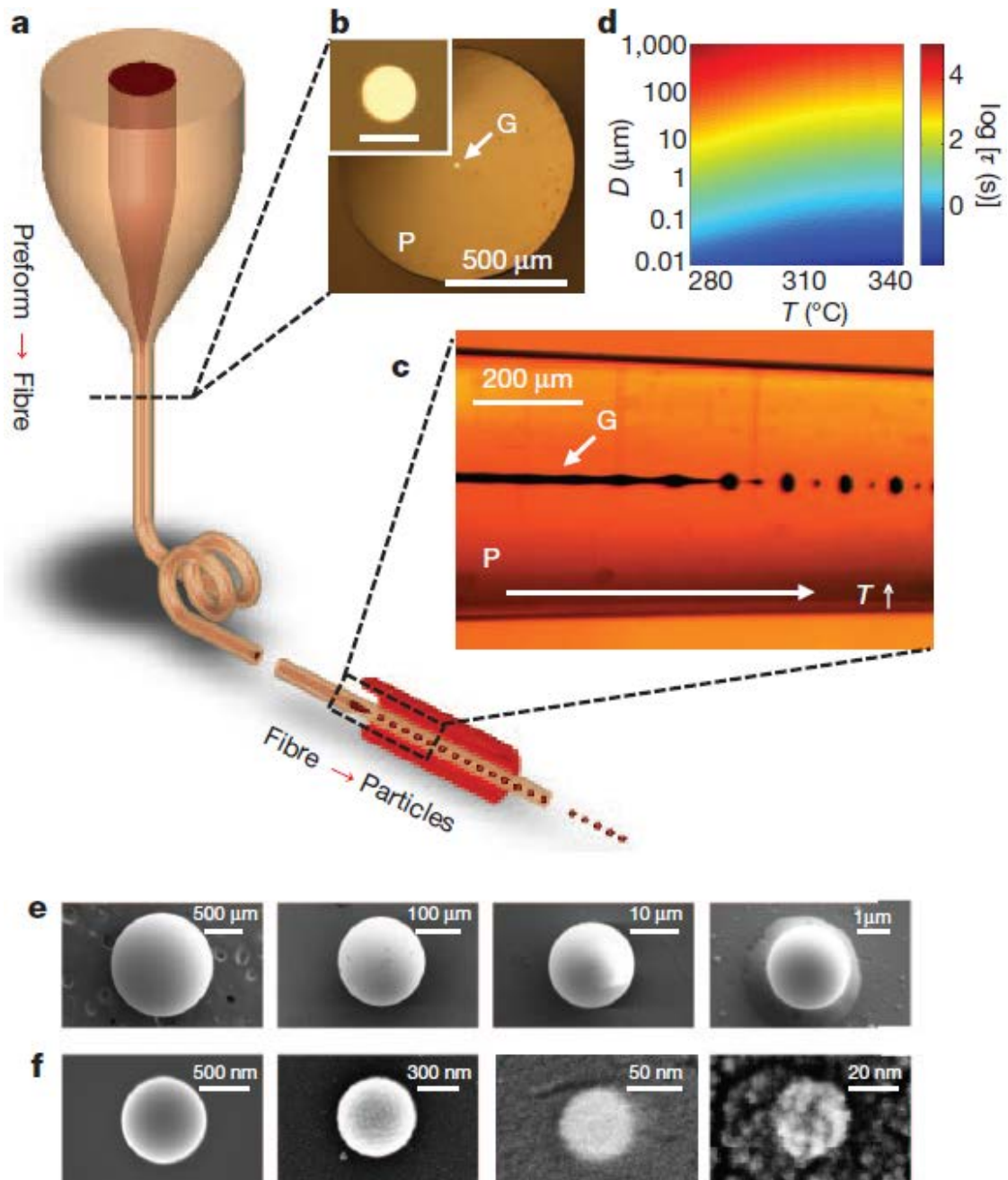
Figure 1. Fluid capillary instabilities in multimaterial fibers as a route to size-tunable particle fabrication. a, A macroscopic preform is thermally drawn into a fiber. Subsequent thermal processing of the fiber induces the PRI, which results in the breakup of the intact core into spherical droplets that are frozen in situ on cooling. b, Reflection optical micrograph of a fiber cross section with 20-mm-diameter core; inset shows the core (scale bar, 20 mm). The fiber consists of an As_2Se_3 glass core (G), encased in a PES polymer cladding (P). c, Transmission optical micrograph of the fiber side-view in b after a temperature (T) gradient is applied along the axis to induce the PRI at the core–cladding interface. d, Calculated instability time, τ, for various temperatures T and core diameters D. e, SEM images of microparticles with diameters of,1.4mm, 200 mm, 18 mm and 2.7 mm. f, SEM images of nanoparticles with diameters of ,920, 560, 62 and 20 nm.

6

An important characteristic of any particle synthesis process is the polydispersity of the particle sizes produced. The mean particle size produced in our process depends on the core diameter of the fiber used. The particle-size distribution around the mean depends on several factors:

1. The uniformity of the core diameter along the fiber axis: this factor may be improved by optimizing the fiber drawing parameters.

2. The uniformity of the diameters of the multiple cores included in the stack-and-draw process: This step relies on the uniformity of the previously drawn fibers that are stacked into the new preform. The uniformity of these fibers was addressed in the point above.

3. The uniformity of the temperature distribution in the heating zone of the furnace used in the thermal processing that induces the PRI-driven breakup. This may be improved by optimizing the geometry of the furnace used.

4. Finally, statistical fluctuations that initiate the breakup process result in concomitant residual fluctuations in the particle-size distribution.

I have determined the polydispersity of three different particle distributions resulting from the breakup of the cores in three different fibers. The results are shown in Fig. 2. The particle-size distributions were determined using the standard technique of dynamic light scattering (DLS) performed using a Malvern Zetasizer Nano ZS system. The particles were extracted from the polymer matrix using DMAC and remained suspended in the DMAC solution inside a quartz glass cuvette that was placed in the DLS system. The three particle distributions had average values of diameter $\langle d \rangle$ of $\langle d1 \rangle = 3.46$ µm, $\langle d2 \rangle = 1.08$ µm, and $\langle d3 \rangle = 557$ nm. The standard deviation of each particle distribution σ normalized with respect to the average diameter, $\sigma/\langle d \rangle$,

was found to be $\sigma1/\langle d1\rangle = 11.3$ %, $\sigma2/\langle d2\rangle = 9.9$ %, and $\sigma3/\langle d3\rangle = 15.8$ %. The higher standard deviation of the smaller diameter particles is attributed to the non-uniformity in the sizes of the large number of stacked cores assembled in the preform compared to the smaller number of cores assembled in the larger-sized-core fiber. The data presented in Fig. 2 is the raw data, and I did not utilize any of the standard techniques for particle-size purification (for example, centrifuging the particles).
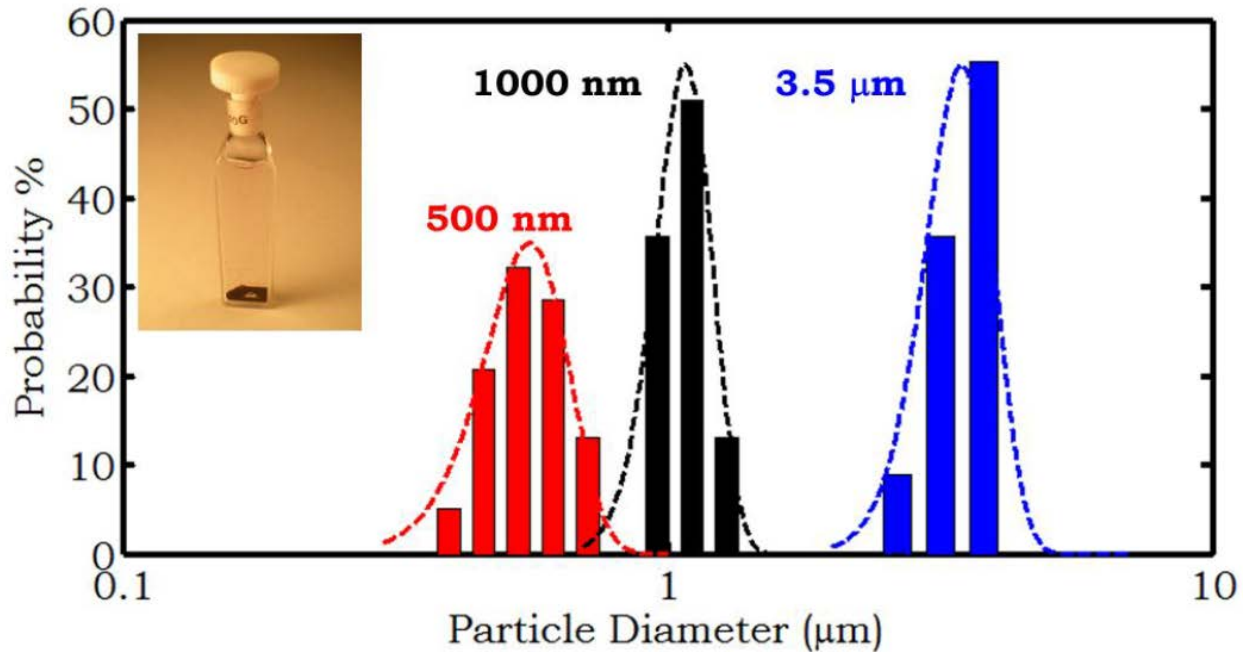
Figure 2. Dynamic light scattering (DLS; Malvern ZetasizerNano ZS) measurements for particles from three representative fibers.The cladding in each case was dissolved using DMAC and the resulting particles were suspended as a dilute colloid in a DMAC solution.Inset is a photograph that shows an example of the particles in the DMAC solution.The three particle distributions haveaverage diameter values $\langle dd1\rangle$=3.46μm, $\langle dd2\rangle$=1.08μm, and $\langle dd3\rangle$=557nm. The standard deviation of each distribution with respect to the average diameteris$\sigma\sigma1\langle dd1\rangle$=11.3⁄%, $\sigma\sigma2\langle dd2\rangle$=9.9⁄%, and $\sigma\sigma3\langle dd3\rangle$=15.8⁄%

1.2 Scalability of Particle Generation

The second key aspect of the in-fiber process is its scalability—that is, the ability to produce large numbers of particles by parallelizing the simultaneous breakup of a high density of cores occupying the same long fiber. Starting from a macroscopic rod, one may in principle convert its entirety into particles of prescribed size. Using a stack-and-draw approach, I have produced fibers of 1 mm outer diameter, containing 12 20-mm cores (Fig. 3a), 4,000 500-nm cores, or 27,000 200-nm cores. In principle, one may combine 10^8 50-nm cores in such a fiber with 25% fill factor. This far exceeds the current parallelization capabilities of microfluidics-based approaches[40]. Furthermore, the resulting spatial distribution of particles held immobilized in the scaffold is well-ordered in three dimensions. In the axial direction the particles are ordered because the instability growth is dominated by a single wavelength. In the transverse dimensions, order is imposed on the cores during the stacking process.
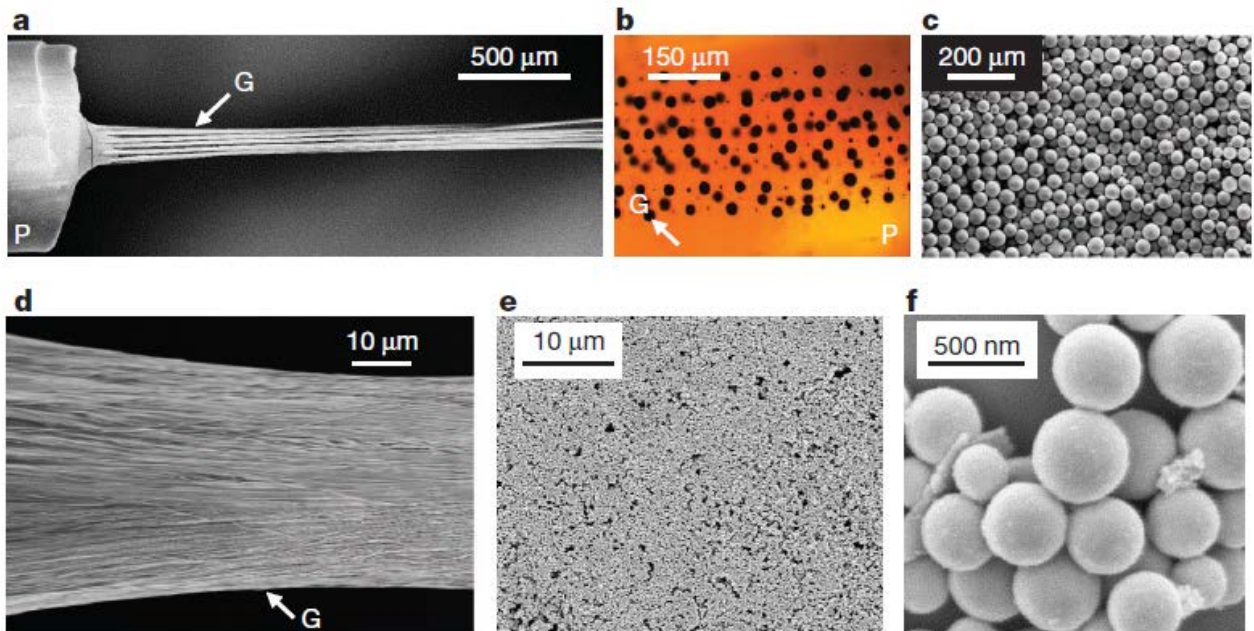
Figure 3. Scalable fabrication of micro- and nano-scale spherical particles. a, SEM image of 12 20-µm intact glass cores (G, As₂Se₃), exposed from a 1-mmdiameter fiber after dissolving the polymer cladding (P, PES). b, Transmission optical micrograph of the fiber side-view, showing the cores after global heating of the fiber, which results in the simultaneous breakup of the cores

into an ordered distribution of particles in three dimensions held in the polymer cladding. c, SEM micrograph of a large number of 40-mm (average diameter) glass particles released from the fiber in b by dissolving the polymer cladding. d, SEM image of 27,000 200-nm-diameter intact glass cores exposed from a 1-mm-diameter fiber. e, SEM image of a large number of 400-nm (average diameter) glass particles. f, SEM image of a few particles from e.

The stack-and-draw process enables me to produce an orderly arrangement of multiple cores in the transverse cross section of the fiber. Furthermore, it allows me to increase the scalability of the process by increasing the percentage of the core material in the fiber cross section. I show below SEM images of the cross sections of the fiber used in Fig. 3, and other fibers, that reinforce this point. First, in Fig. 4 I show the cross section of the 12-core fiber used in Fig. 3a-c. Next I show in Fig. 5 the cross section of the fiber used in Fig. 3d-f.A higher-magnification SEM micrograph of this fiber is shown in Fig. 6 which highlights the orderly arrangement of the stacked cores. The fibers from a previous draw are stacked in a hexagonal lattice and on each lattice site 80 cores (each 200-nm in diameter) are arranged in a circular lattice.
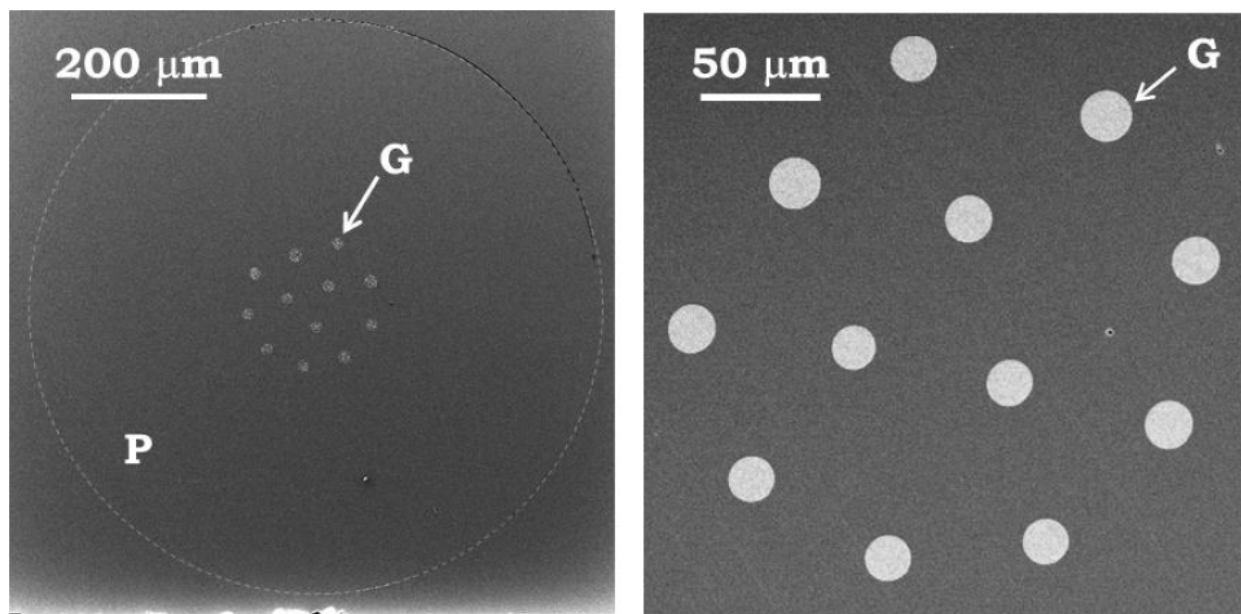
Figure 4. SEM micrograph of the cross section of the 12 20-µm-diameter-core fiber (left) used in Fig. 3a-band a higher-magnification SEM micrograph of the cores (right).G: glass (As2Se3); P: polymer (PES).
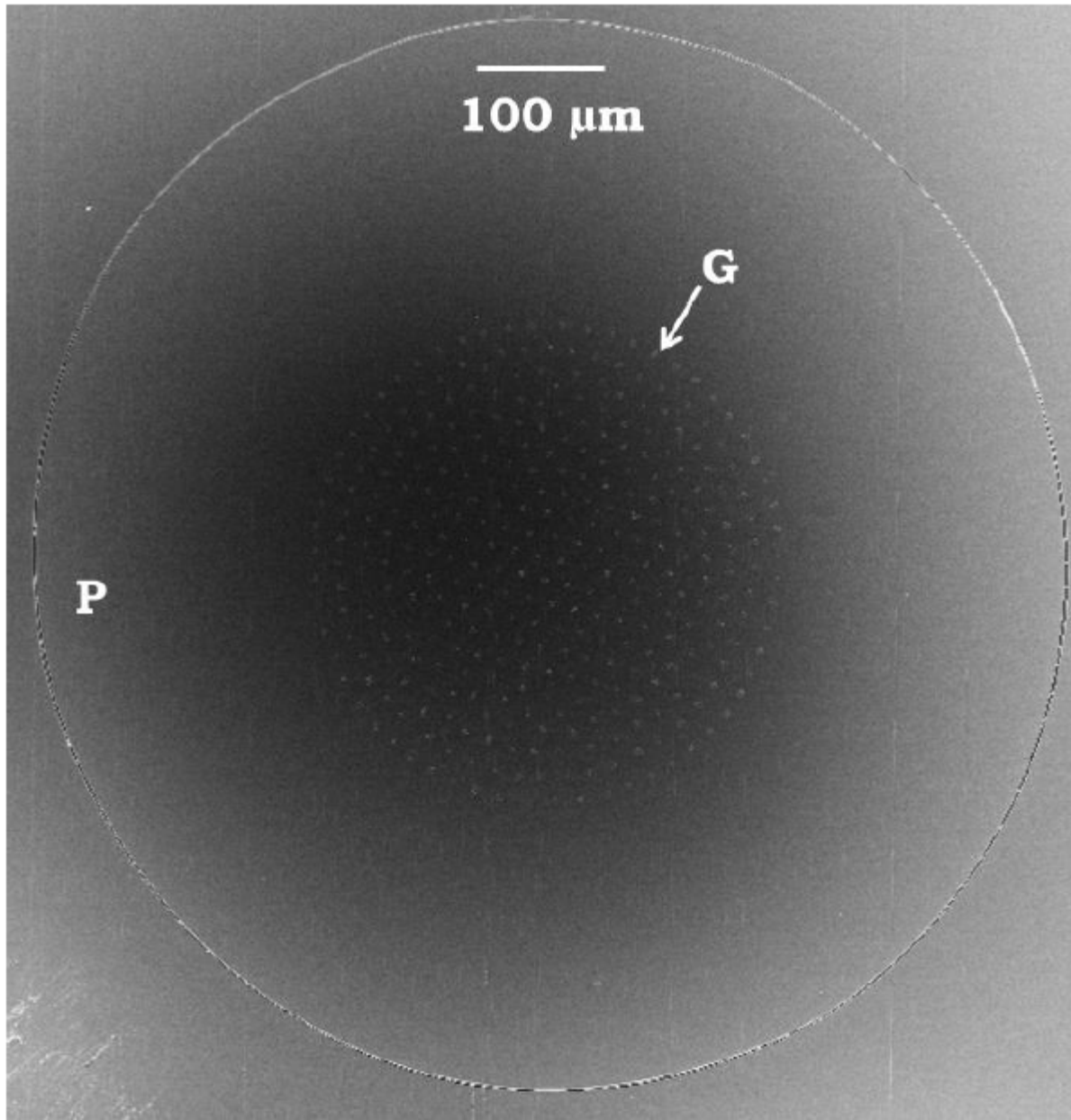
Figure 5. SEM micrograph of the cross section of the 27,000 200-nm-diameter-core fiber used in Fig. 3d.The fiber consists of ~ 330 stacked fibers each containing 80 cores drawn into the shown fiber. P: polymer (PES).
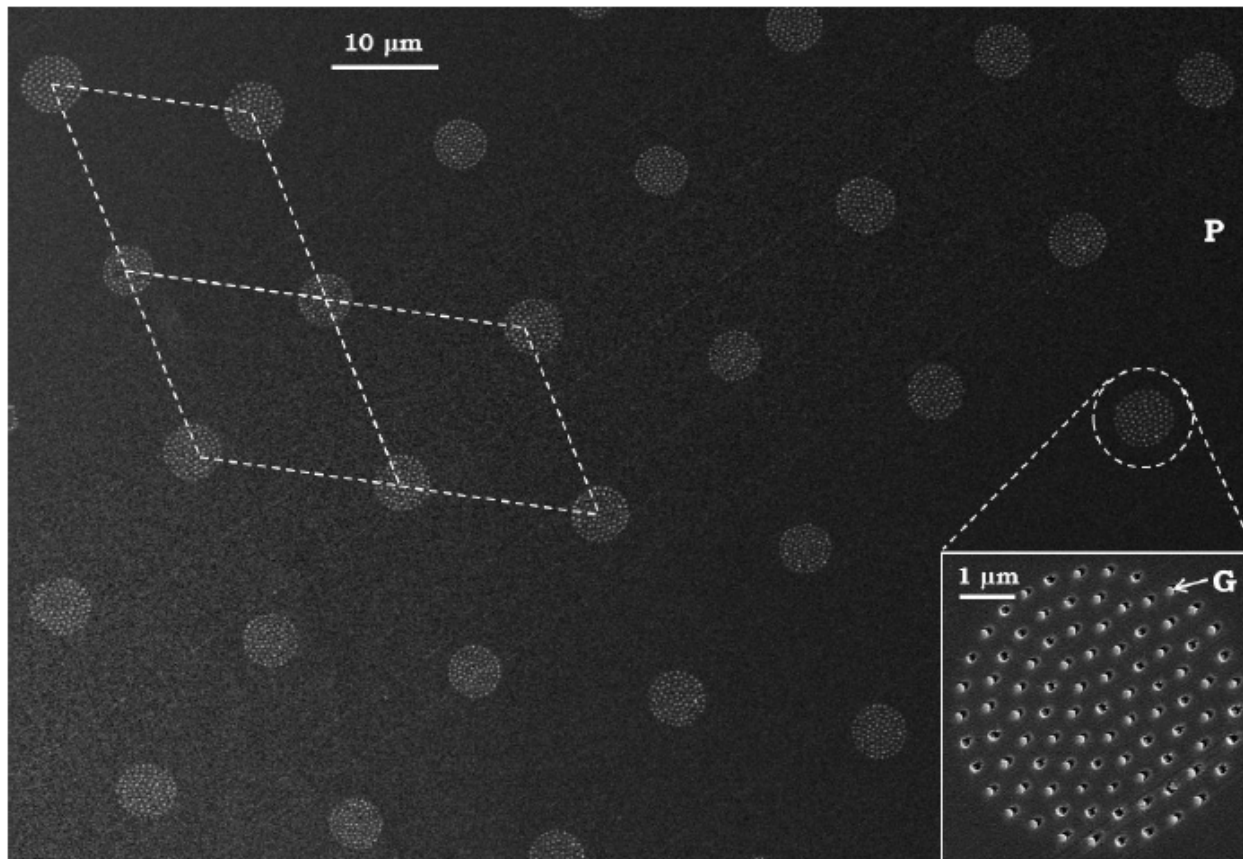
Figure 6. Higher-magnification SEM micrograph of a portion of the fiber core in Fig. 3. The stacked fibers in the preform produce a hexagonal lattice. At each lattice site 80 200-nm glass cores are located as shown in the inset.G: glass (As2Se3); P: polymer (PES).

After breakup via the thermally induced PRI, each core breaks up into a necklace of spherical particles with period governed by the physical parameters. Therefore, the three-dimensional arrangement of the particles in the polymer cladding matrix is periodic in all three dimensions. The periodicity in the two transverse dimensions is imposed by the stacking process and the longitudinal periodicity of each core is a result of the physics of the PRI process. This is highlighted in Fig. 7. The order in the axial direction is less controllable than in the transverse directions for two reasons. First, the periodicity of the PRI-driven breakup is not exact due to non-uniformities in the thermal distribution. Second, the breakup of different cores is independent when they are sufficiently separated from each other. Therefore, the periods of the breakup in the cores do not necessarily line up. Decreasing the separation between the cores

12

leads to coupling between the breakup processes which may lead to correlated or anti-correlated periods in adjacent cores. This may lead to an efficient process to produce three-dimensional photonic crystals and metamaterials.
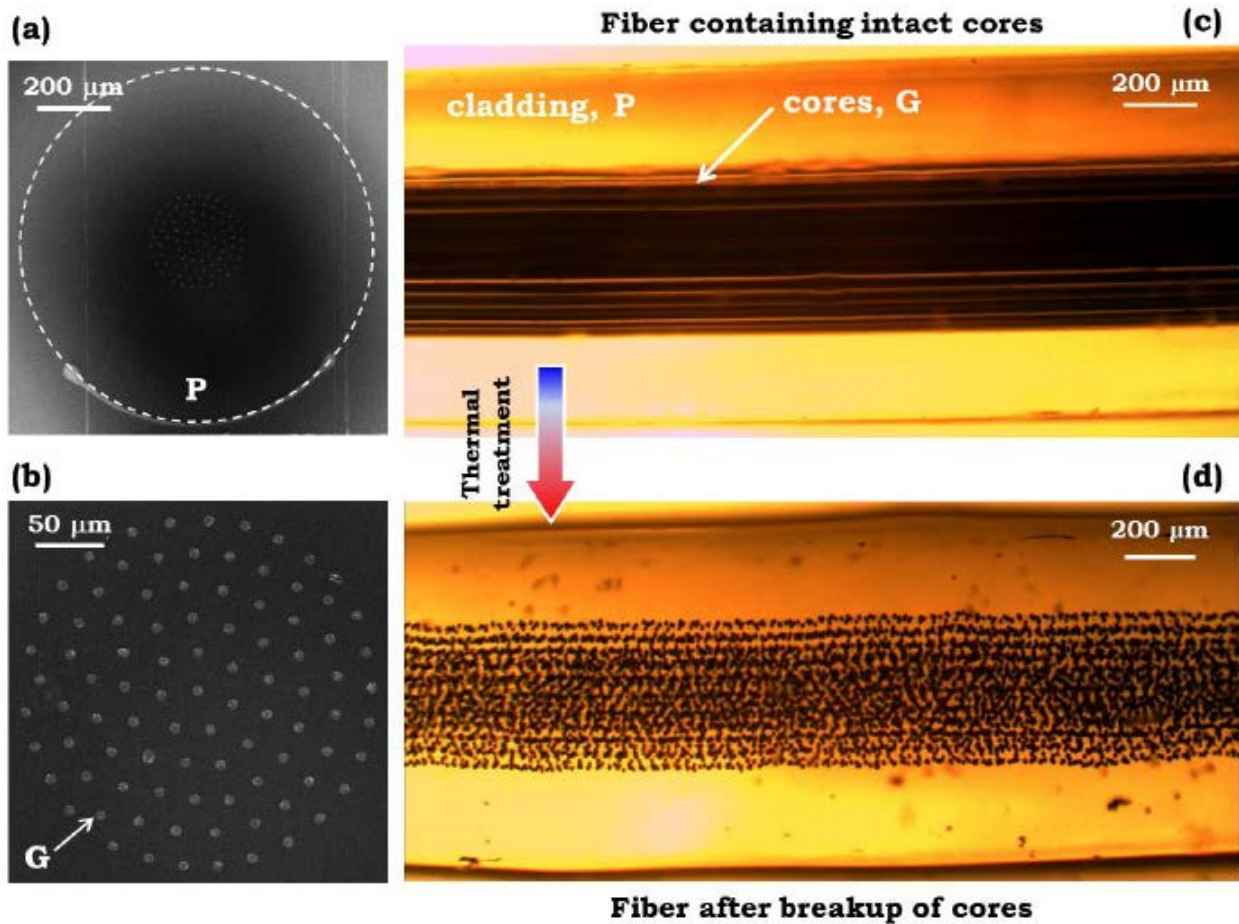
Figure 7. Well-ordered, three-dimensional particle emulsion held in the polymer cladding. (a) SEM micrograph of a 1-mm-diameter fiber cross section containing 80 7-µm-diameter cores. (b) Higher-magnification SEM micrograph of the 80 cores. G: glass (As2Se3); P: polymer (PES). Transmission optical micrographs of the fiber side view(c) before and (d) after breakup (via global heating) showing the 3D well-ordered particle emulsion.

1.3 Structured Particles

The third characteristic is the ease by which this top-down process may be configured to produce structured particles. Because the preform is constructed at the centimeter scale, complex preform geometries may be readily designed and realized, so that the PRI-driven breakup in the drawn fiber

produces a desired particle structure. I have demonstrated the size-controllable fabrication of spherical core–shell particles (Fig. 8) and 'Janus' particles (Fig. 9). The preform used to produce the core–shell particles (corresponding to a double emulsion[9]) consists of a polymer core (diameter D_1) and glass cladding (diameter $D_2 \sim 2.53D_1$), surrounded by a polymer scaffold (Fig. 8a; cross sections shown in Fig. 8b, c). The preform this fiber was drawn from was produced by extruding a 30-mm diameter cylindrical billet through a circular die (12-mm diameter). The billet consists of three discs: top disc is polymer, middle disc is glass, and bottom disc is again polymer, with heights 30, 20, and 20 mm, respectively. The billet is heated to above the softening temperature and then pushed vertically downward through the die under pressure. The extruded rod was then used as a preform to draw fibers (cross sections in Fig. 8b-c). Upon heating, the polymer core and glass shell undergo a correlated PRI-driven breakup that results in core–shell particles, observed experimentally (Fig. 8d, e) and confirmed through simulations (Fig. 8f). To confirm that the PRI-driven breakup produces the expected structure, I use a focused ion beam (FIB) to 'slice' the particle down the middle by raster-scanning the FIB across a box with an edge lying through the particle. The FIB etches the semiconducting glass shell, with its higher electrical conductivity, more effectively than the insulating polymer core. Figure 8g, h shows SEM images of particles with outer diameters from 35 μm to 600nm (the FIB damages the smaller particles that we produced), showing the intact polymer core protruding from the remaining glass half-shell. Figure 8g, h confirms the smooth core/shell interface, the particles' concentric spherical surfaces, and that the expected core/shell diameter ratio, $D_1'/D_2' = (D_1/D_2)^{2/3}$, as dictated by conservation of volume (where D_1' and D_2' are the particle core and shell diameters, respectively). Since $D_1/D_2 = 0.4$ (Fig. 8b, c), it is expected that $D_1'/D_2' \sim 0.543$, in close agreement with the measured value of ~ 0.575 (Fig. 8g).

The second structured particle I produced is a broken-symmetry, spherical Janus particle, comprised of two hemispheres of different optical glasses (Fig. 9). The preform core is constructed of two half cylinders, each of a different optical glass: G1 (As_2S_3) and G2 ($(As_2Se_3)_{99}Ge_1$) (Fig. 9a–c). The two

glass half cylinders (12-mm diameter, 30-mm long) were produced by melt-quenching. The two optical glasses have approximately similar viscosities at the target particle breakup temperature ($\sim 350\ °C - 400$ °C). A cylinder was formed from the two glass half-cylinders and was then used as the core of a preform by rolling a PES thin film around it followed by consolidation under vacuum. The 30-mm diameter preform was then drawn into the fibers used for Janus-particle fabrication (Fig. 9).The induced breakup produces spherical Janus particles held immobilized with the same orientation in the cladding (Fig. 9d). Figure 9e shows a reflection optical micrograph of a single Janus particle removed from the cladding. I confirmed the three-dimensional structure of the particle by optically imaging multiple parallel planes cutting through a particle still embedded in the polymer cladding (Fig. 9f), and correlating the optical images with energy-dispersive X-ray diffraction (EDX) spectral images of the particle cross-section (Fig. 9g) that identify arsenic and sulphur. The measurements confirm the three-dimensional, two-compartment structure of the Janus particle.

Modeling Janus-particle formation is difficult because it involves a point where three fluids meet, so that sophisticated level-set techniques are required to describe the interfaces[41]. The physics of such a contact point is not well understood[42], although it is likely to be less relevant in the Stokes regime[43,44]. Nevertheless, energy considerations yield some qualitative predictions. A large glass–glass surface tension, compared to that between glass and polymer, would make it energetically favorable for the Janus particles to pinch in the center. On the other hand, for negligible glass–glass tension, if the glass–polymer surface tension were very different for the two glasses, energy would be lowered if one glass were to flow to envelop the other. As neither of these scenarios is observed experimentally (Fig. 9d, e), I can conclude that the observed breakup process is consistent with low glass–glass surface tension and similar glass–polymer tensions. These considerations indicate a general strategy for the construction of particles with even more complex geometry. Furthermore, to form two-component particles, the viscosities of the two

materials must be matched; I identify pairs of compatible materials by looking for overlapping softening temperatures.

Figure 8. Polymer-core/glass-shell spherical particle fabrication. a, Schematic of the fiber structure (P, G as in Figs 1, 2). b, c, SEM images of fiber cross-sections. d, SEM image of the glass-shell outer surface, showing the modulation characteristic of the PRI. e, SEM image of the structure in d after sectioning off half of the glass shell using a focused ion beam (FEI 200 THP; current ,10–100 pA), revealing the correlated modulations on the two interfaces (inner polymer/glass and outer glass/polymer

interfaces), and resulting ultimately in two concentric spherical surfaces as shown in g and h. f, Three snapshots from a three-dimensional simulation of the Stokes equations using a representative fiber structure, illustrating the full breakup process. Time progresses from top to bottom. Scale bar, 50 mm. Dark green, polymer core; light green, glass shell; the outer polymer scaffold cladding is made transparent for clarity. g, Top and h, front (tilted) SEM views of four differently sized core–shell particles (outer diameters 34 mm, 7 mm, 1.2 mm and 650 nm, respectively). Scale bars in the corresponding top and front views are the same length.

Figure 9. Broken-symmetry Janus particle and 'beach ball' particle fabrication. a, Schematic of the Janus preform. G1,As_2S_3; G2, $(As_2Se_3)_{99}Ge_1$; P, PES. b, Reflection optical micrograph of a Janus fiber cross-section; scale bar 20mm. c, Transmission optical micrograph of the fiber side view. d, Transmission optical micrograph showing PRI growth, leading to breakup of the Janus particles. e, Reflection optical micrograph of an individual Janus particle after removal from the fiber. f, Optical micrographs of

17

multiple sections at different depths within a single Janus particle embedded in the fiber, exposed sequentially by polishing. The particle symmetry plane is tilted with respect to the direction of polishing, and the tilt is similar to that in the particle shown in e. g, EDX spectral images (for arsenic, As, and sulphur, S) of an exposed Janus particle cross-section, corresponding to a section from f. The dashed blue circle and line are visual aids. h, Schematic of the preform to produce 'beach ball' particles; G1, G2 and P as above. i, Reflection optical micrograph of a 'beach ball' fiber cross-section; scale bar, 20mm. j, EDX spectral images (as in g) of an exposed 'beach ball' particle cross-section. k, Transmission optical micrographs of the cross-sections of a 40-mm-diameter particle immobilized in the polymer matrix in the fiber; scale bar 20mm.

The two particle structures considered above, the core–shell and two-compartment Janus particles, are prototypical structures from which more complex geometries may be constructed. For example, multilayer particles may be produced using a core consisting of nested cylindrical shells of appropriate thicknesses, and additional azimuthal compartments in the particle result from a core appropriately prepared with azimuthal sections. Furthermore, these two prototypical structures may be combined in the same particle. The power of this approach is highlighted in Fig. 9h–k, which shows the fabrication of a 'beach ball' particle, consisting of six equally sized wedge-shaped sections of alternating materials (G1 and G2). The preform consists of a cylindrical core with six equally sized segments, each subtending a 60 degree polar angle. More complex particle structures may be produced by judiciously structuring the core.

CHAPTER 2 POLYMER PARTICLE FABRICATION

2.1 All-Polymer Fiber Fabrication and Particle Release

All of the particles discussed so far result from the PRI developing at a polymer-glass interface. Additionally, all of the particles produced were made entirely of glass (excluding the polymer core of the core-shell particle). While using these materials was useful for showing the ability to produce complex particles in a large size range and in a scalable way, the method would be even more powerful if it could be extended to all-polymer fibers. Having a single process that could maintain the advantages discussed above but for many materials would be extremely beneficial. For example, polymeric micro- and nanoparticles are becoming a mainstay in biomedicine, medical diagnostics, and therapeutics, where they are used in implementing sensing mechanisms, as imaging contrast agents, and in drug delivery. Current approaches to the fabrication of such particles are typically finely tuned to specific monomer or polymer species, size ranges, and structures. I have shown that the in-fiber PRI method can produce uniformly-sized spherical polymeric particles from a wide range of polymers produced with complex internal architectures and continuously tunable diameters extending from the millimeter scale down to 50 nm. Controllable access to such a wide range of sizes enables broad applications in cancer treatment, immunology, and vaccines. I have demonstrated surface functionalization of the extracted particles for biodetection through specific protein–protein interactions, volumetric encapsulation of a biomaterial in spherical polymeric shells, and the combination of both surface and volumetric functionalities in the same particle. These particles used in distinct modalities may be produced from the desired biocompatible polymer by changing only the geometry of the macroscopic preform from which the fiber is drawn.

19

The process for fabricating polymeric particles is identical to that of the glass particles. The only slight difference is that glass is chemically different enough from polymer such that nearly any organic solvent will dissolve the cladding polymer without affecting the glass particles. When the particles are also polymeric, care must be taken to find a solvent that will dissolve the cladding polymer without affecting the particle material. The three processing stages are illustrated in Fig. 10a, where a preform consisting of a 700-µm-diameter cylindrical cyclic olefin polymer (COP)[45] core surrounded by a 35-mm-diameter polysulfone (PSU) cladding (stage I) is thermally drawn into hundreds of meters of a uniform 1-mm-diameter fiber with a 20-µm-diameter core (stage II; Fig. 10b). The drawn fiber is thermally treated under ambient conditions, thereby reducing the material's viscosity and inducing the PRI (stage III), whose dynamics are shown in Fig. 10c. After breakup, I extract the COP particles by selective dissolution of the PSU cladding [using dimethylacetamide (DMAC)]. Note that the dissolved cladding polymer may be recycled from the solution and reused as a cladding for a new fiber. Figure 10d shows scanning electron micrographs of representative examples of particles with diameters extending three orders of magnitude from ∼50 µm down to ∼50 nm. Just as in the case with the glass particles, the scalability may be enhanced by using the stack-and-draw process, as shown in Fig. 12.
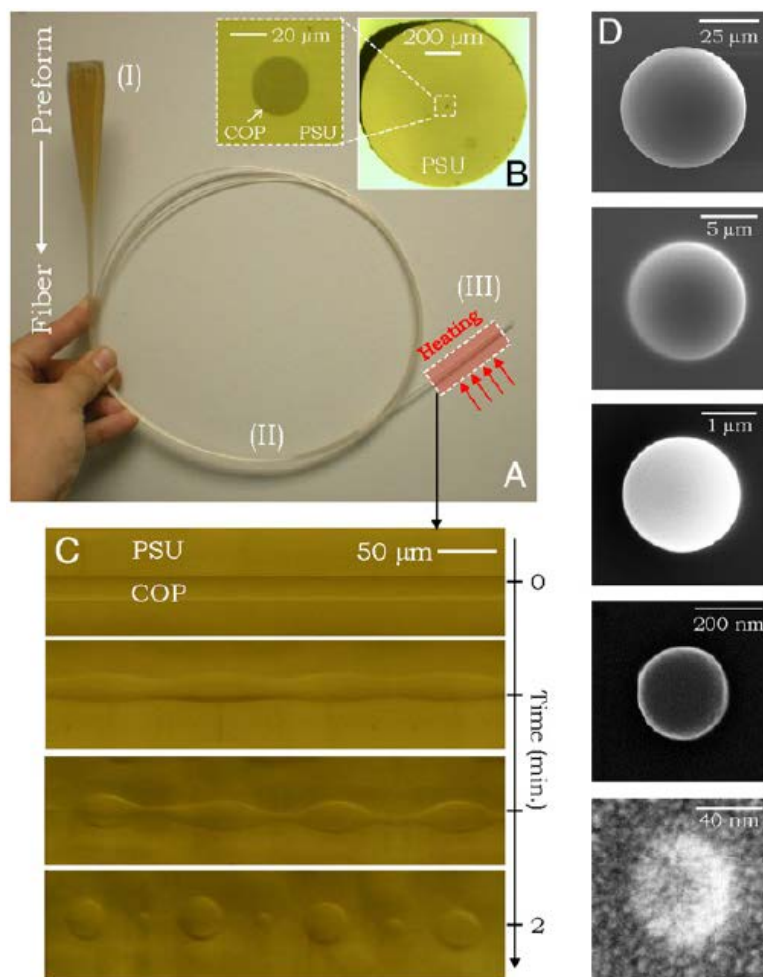
Figure 10. In-fiber emulsification as a route to producing spherical polymer particles. (A) Preform-to-fiber approach. A centimeter-scale preform (Upper Left) is drawn into a 1-mm-diameter fiber. The Roman numerals identify the three fabrication stages outlined in the main text. (B) Optical transmission micrograph of the fiber cross-section consisting of a 20-μm-diameter COP core inside a PSU cladding. (C) Side views of a section of a fiber undergoing thermal reatment at 321 °C showing the temporal evolution of the PRI starting from the intact cylindrical COP core until it breaks up into a necklace of particles embedded in the PSU cladding. (D) Size tunability of COP particles, released from the PSU cladding using DMAC, demonstrated in scanning electron micrographs. [Scale bar: D, successively educed by a factor of 5 (Upper to Lower)]. Particle diameters are ∼53 μm, 10.6 μm, 2.2 μm, 270 nm, and 61 nm.

I have confirmed that this method is not unique to the PSU/COP materials system by producing particles from a wide range of polymers, including polystyrene (PS, Fig. 11), acrylonitrile butadiene styrene (ABS, Fig. 11), polycarbonate (PC), polyetherimide (PEI), and polyethersulfone (PES). These polymers have very different biochemical, mechanical, and optical characteristics, and some of them (e.g., COP and ABS) have yet to be produced in particle form. For example, ABS at room temperature is

21

a rigid polymer, but its characteristics at room temperature do not come into play during breakup under thermal treatment. Although PS is extensively used in biomedicine due to its low density (allowing for suspension of PS particles in aqueous solutions) and its chemical inertness, COP maintains these characteristics with the additional benefits of its excellent protein adsorption characteristics[46] and resistance to many more chemicals than PS, such as acids, alkalis, and most organic polar solvents (e.g., acetone, methanol, isopropyl alcohol)[47].
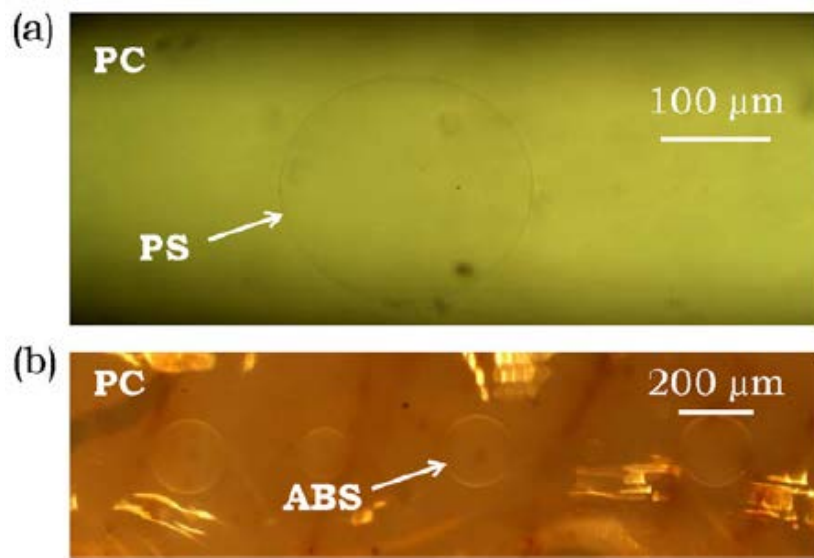
Figure 11. (A) Transmission optical micrograph of a single PS particle in a 1-mm-o.d. PC cladding. The diameter of the particle is ~250 μm. (B) Reflection optical micrograph of a string of spherical ABS particles held in a 1-mm-o.d. PC cladding. The diameter of the particles is ~150 μm.
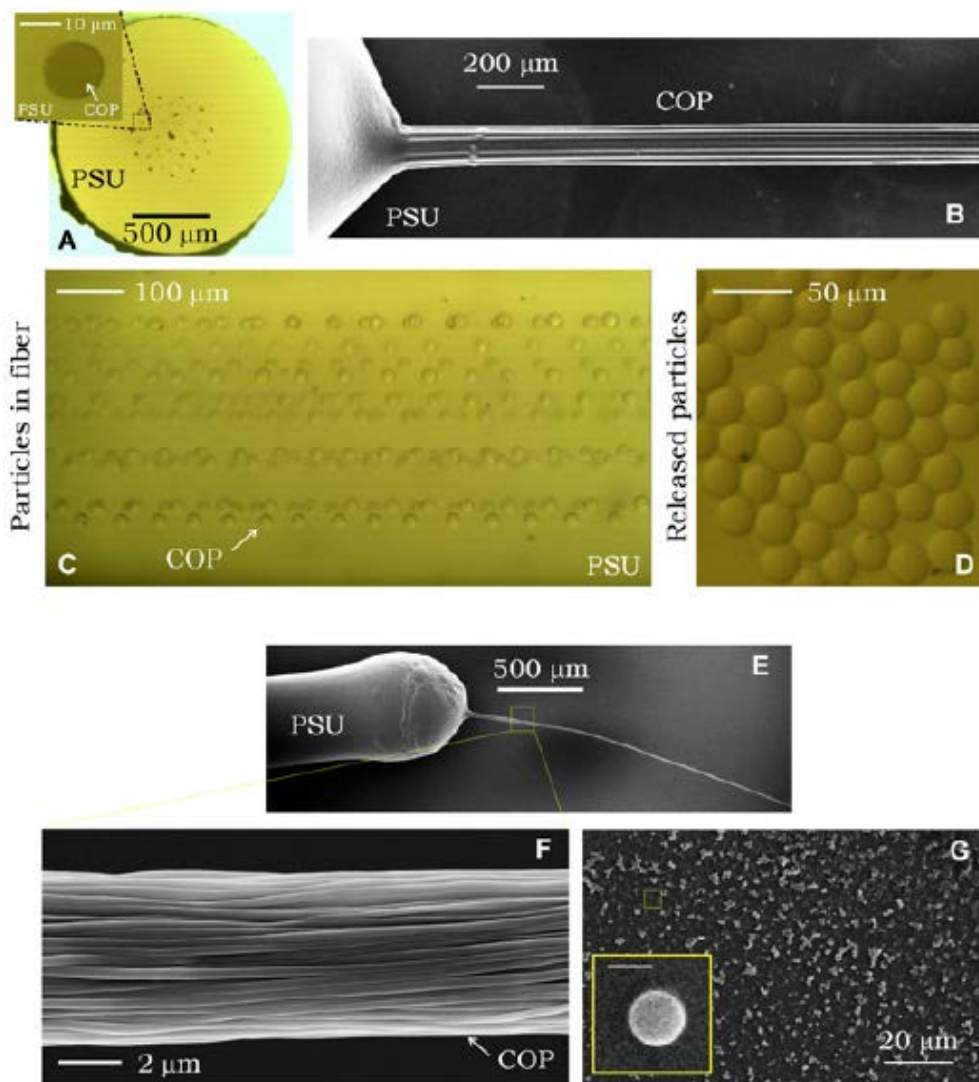
Figure 12. Scalable in-fiber emulsification. Microscale (A–D) and nanoscale (E–G) in-fiber emulsification. (A) Optical transmission micrograph of the cross section of a 14-core fiber with 20-µm-diameter COP cores in a PSU cladding. (Inset) Individual core cross-section. (B) Scanning electron micrograph of the fiber side view showing the 14 intact COP cores after dissolving the PSU cladding. The cores coalesce after removing the fiber from the solvent. (C) Optical transmission micrograph of the fiber side view after thermally inducing the PRI, resulting in the cores breaking up into spherical particles held stationary in the cladding matrix. (D) Optical transmission micrograph of the released COP particles after dissolving the PSU cladding. (E and F) Scanning electron micrographs of 1,000 intact 500-nm-diameter COP cores emerging from the fiber after dissolving the PSU cladding matrix. (G) Scanning electron micrograph of the released COP particles. (Inset) Scanning electron micrograph of a single particle. (Scale bar: 500 nm.)

23

2.2 Structured Polymer Particle Fabrication

In the previous chapter I discussed the fabrication of structured glass particles. To show that this structuring is not exclusive to glass particles, two structured particle geometries are made from all-polymer systems: core-shell and Janus. The all-polymer core-shell particle fabrication was as follows: The PC-shell/COP-core particles were fabricated using the following steps: (i) A 4.5-mm diameter cylindrical rod of COP was extruded at 240 °C; (ii) a preform was constructed by rolling 75-μm-thick sheets of PC around the rod until its diameter reached 6.5 mm (corresponding to the shell), followed by rolling 75-μm-thick sheets of COP until the final diameter reached 30 mm (corresponding to the fiber cladding), after which it was consolidated under vacuum at 150 °C; (iii) the preform was thermally drawn down to a thick cane with a diameter of 4 mm at 250 °C; (iv) 75-μm-thick sheets of COP were rolled around this cane until its diameter reached 25 mm, and the structure was again consolidated under vacuum; (v) this new preform was then drawn down to a 1-mm-diameter fiber, such that the inner COP core was ~25 μm; and (vi) the fiber was thermally treated in an oven at 350 °C for 3 min to induce the Plateau–Rayleigh capillary instability (PRI) (Fig. 13).
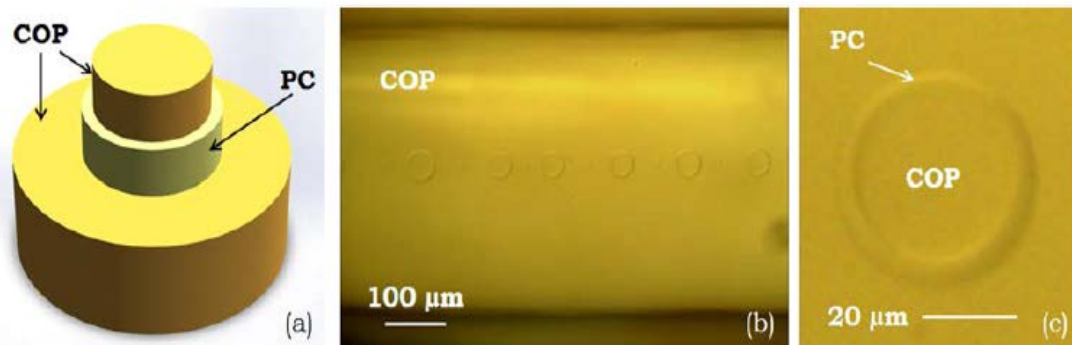
Figure 13. (A) Schematic of the structure of the preform/fiber cross-section used to produce core/shell polymer particles. (B) Optical transmission micrograph of the fiber side view showing COP-core/PC-shell particles held in a COP cladding matrix. (C) Higher magnification transmission micrograph of a single core/shell polymer particle.

The fabrication of the all-polymer Janus particles was as follows: The fiber preform used to produce polymer Janus particles was produced by multimaterial coextrusion (1). The cylindrical extrusion billet was formed of a cylindrical core and two cladding layers. The core was a 6-mm diameter rod formed of two half-cylinders: one PES and the other polyetherimide (PEI; Ajedium), constituting the Janus core. Each half-cylinder was produced by machining a 6-mm diameter rod of each polymer produced by extrusion. The first billet cladding was a 6-mm-i.d. and 12-mm-o.d. tube of the chalcogenide glass, As2S3, produced by extrusion from a 30-mmdiameter As2S3 disk (Amorphous Materials, Inc.). The second cladding layer was a PES tube (12-mm i.d., 30-mm o.d.) prepared by rolling a 125-μm-thick PES film, followed by thermal consolidation at 245 °C under vacuum. The resulting extrusion billet had the form of a 30-mm-diameter, 30-mm-high cylinder. Extruding this billet produced a 6-mm-diameter rod. We further provided a larger diameter PES jacket by thin-film rolling followed by thermal consolidation at 245 °C under vacuum. The resulting 30-mm-diameter preform was drawn into a 1-mm diameter fiber with a core diameter of 40 μm and an As2S3 outer shell diameter of 80 μm. The fiber was thermally treated in an oven at 400 °C for 2 min to induce the PRI-based breakup. The PES cladding was dissolved with DMAC, and the particles were collected in a watch glass and washed three times in pure DMAC to get rid of any dissolved polymer. Next, a dilute, aqueous NaOH solution was used to dissolve the outer glass layer of the particles slowly and to expose the PEI/PES Janus particles (Fig. 14).
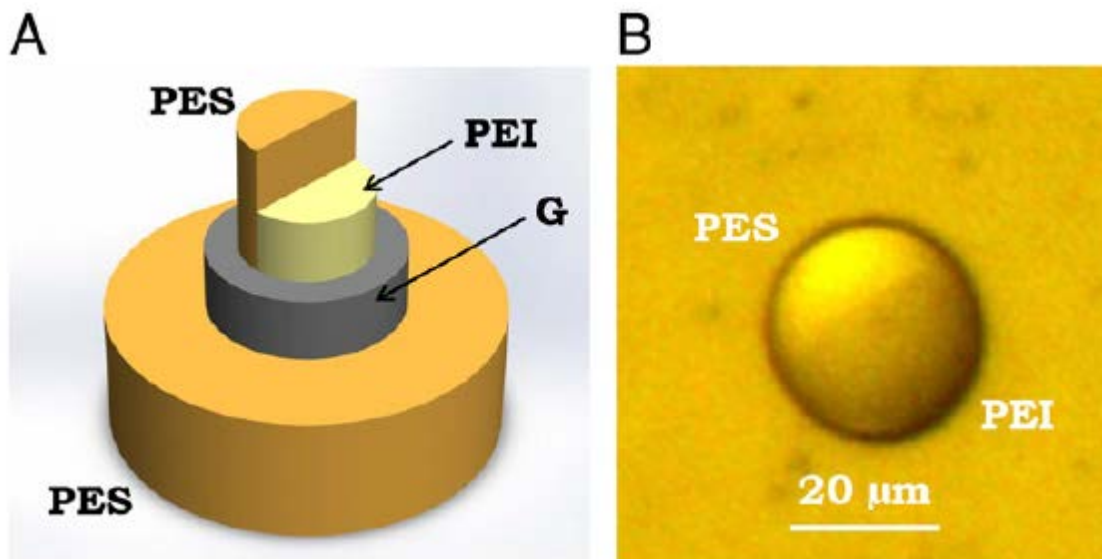
Figure 14. (A) Schematic of the structure of the preform/fiber cross-section used to produce core/shell polymer particles. G is a chalcogenide glass, As2Se3. (B) Optical transmission micrograph of a single Janus particle with PES and PEI hemispheres.

Although the particle formation process itself is independent of the chemistry of the core and cladding materials, extracting the particles by selective dissolution of the cladding, on the other hand, does indeed depend on the chemistry of the fiber materials, which places restrictions on the potential polymeric core/cladding pairings. This constraint is lifted by separating the core and cladding polymers with a thermally compatible inorganic buffer layer added in the preform, in which case the core and cladding may even be the same polymer. We realize this design here using PES in both the core and the cladding separated by a layer of the thermally compatible chalcogenide glass, As_2Se_3[48] (Fig. 15b, c). The PRI yields particles having a core (polymer)/shell (glass) structure that are released by dissolving the polymer cladding (using DMAC), and the polymer particles are extracted by subsequent removal of the shell (using NaOH in deionized water; Fig. 15d).

Applying my general fabrication strategy using different preform structures but the same biocompatible polymer (COP), I have produced two distinct particle structures tuned to two different classes of applications. The first class consists of solid particles that we use for demonstrating surface

26

binding of protein and fluorescent antibodies (FAs), a necessary step for biosensing; furthermore, we verify controllable protein coating of the COP particles while maintaining biological specificity. Using the same fabrication procedure applied to a hollow-core fiber design, a second class of particles is developed for encapsulation of selected materials inside a COP shell. I have demonstrated this feature using collagen as a model biological material, motivated by recent work demonstrating the utility of collagen nanoparticles in skin tissue engineering[49], bone regeneration[50], and treatment of bacterial infection[51].
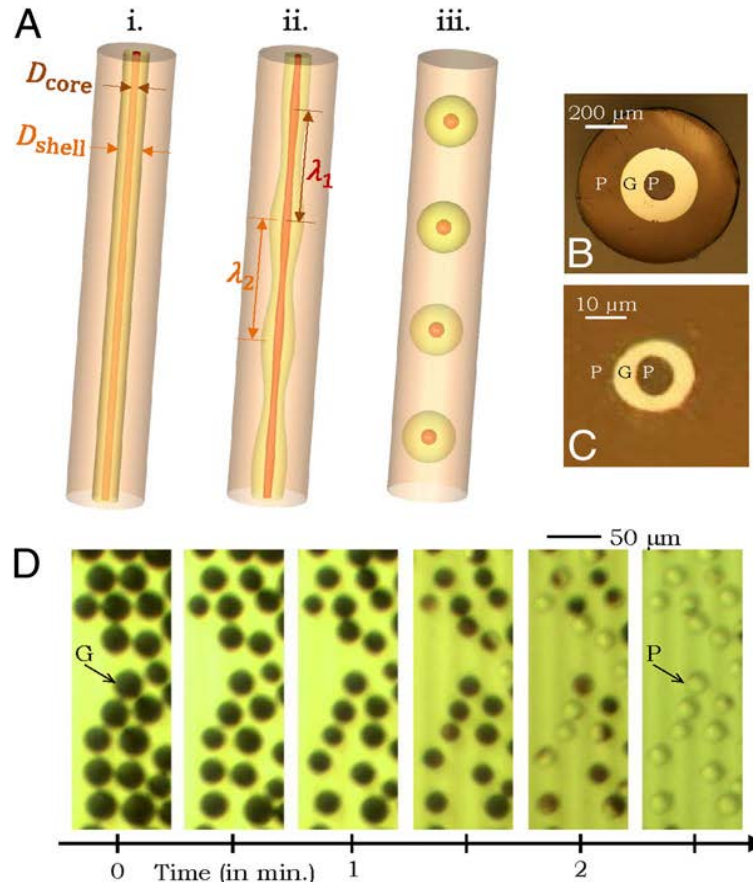
Figure 15. Inorganic sacrificial buffer layer to facilitate particle extraction. (A) Schematic of the fiber structure. (B and C) Optical reflection micrographs of the fiber cross-section at two stages in the fabrication process. The core onsists of a PES (P) cylinder surrounded by a layer of an inorganic glass, As_2Se_3 (G). The core is embedded in a PES cladding matrix. (D) Time-lapse transmission optical micrographs of core (P)/shell (G) particles placed in NaOH solution. The glass shell is dissolved, leaving behind the polymer cores.

2.3 Surface Binding and Encapsulation

I first demonstrate that the surfaces of the polymer particles produced by the fluid instability-based process are amenable to protein binding without pretreatment, and are thus suitable for biosensing applications. By coating solid COP microparticles, removed from the fiber PSU cladding, with antibodies conjugated with fluorophores (FAs) through adsorption, I can directly monitor optically the presence of bound proteins using two readily distinguishable FAs: yellow-fluorescing FA1 [Cy3-conjugated anti-rabbit antibodies produced in goat (gAr); Fig. 16a] and red-fluorescing FA2 [Alexa Fluor-647–conjugated anti-mouse antibodies produced in goat (gAm); Fig. 16b]. It was next verified that the particle-bound proteins retain their native conformation through optical detection of specific protein–protein interactions. The particles were coated with mouse serum proteins and the fluorescence emitted by two FAs incubated with the particles was monitored, one that recognizes mouse serum proteins (FA2, gAm antibodies; Fig. 16d) compared with one that does not (FA1, gAr antibodies; Fig. 16c). Lack of fluorescence from FA1 indicates that mouse serum proteins remain uniformly bound to the particles in their native conformation, thereby preventing FA1 from binding directly to the particles. Moreover, protein binding may be promoted through adding a positive charge to the hydrophobic polymer particle surface by coating it with poly-L-lysine, a positively charged synthetic amino acid chain. This enhancement was confirmed by detecting stronger fluorescence from bound antibodies (compare the panels in Fig. 16a, e) and also by observing Förster resonant energy transfer (FRET) between two tandem layers of particle-bound FAs[52,53] from FA1 to FA3 (Alexa Fluor-647–conjugated anti-goat antibodies produced in donkey). Antibodies FA3 recognize FA1 and fluorescence from FA1 overlaps with the FA3 excitation band, thereby allowing for FRET transfer (Fig. 16e). It was further verified that protein binding is independent of particle diameter down to 500-nm diameters by incubating 500-nm-diameter COP particles (Figs. 16g, f) with FA4 (Alexa Fluor-488–conjugated gAm antibodies).
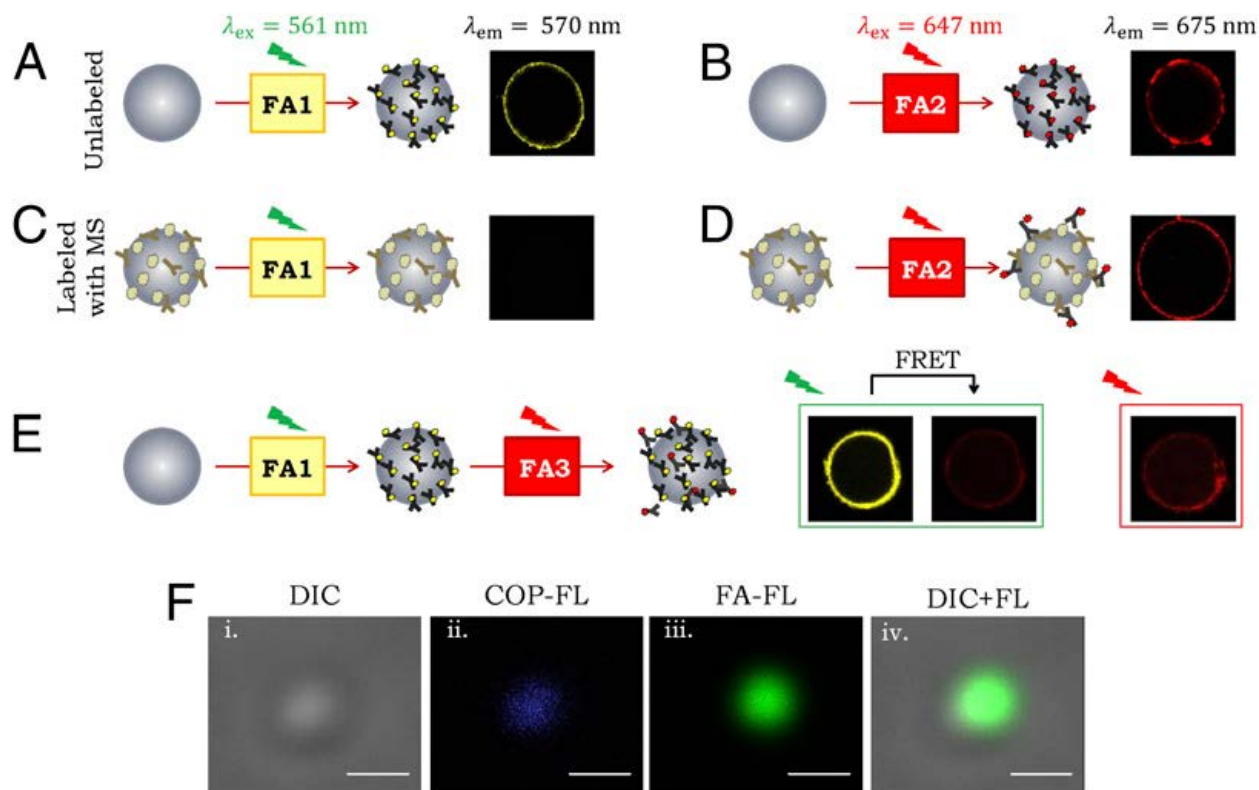
Figure 16. Quantitative assessment of preferential protein coating to polymer particles. (A and B) COP particles coated with FA1 (gAr) or FA2 (gAm) yield yellow or red fluorescence when excited at 561 nm or 647 nm, respectively. Here, λex is the excitation wavelength, λem is the emission wavelength, and green and red arrows correspond to the excitation with λex =561 nm and λex =647 nm, respectively. (C and D) COP particles coated with mouse serum (MS) yield red fluorescence with MS-specific FA2 (gAm) and none with nonspecific FA1 (gAr). (E) COP particles after treatment with poly-L-lysine are coated with FA1 and then FA3 [anti-goat antibodies produced in donkey (dAg), which recognize FA1]. Both antibodies independently produce fluorescence upon excitation. When FA1 is excited (at λex =561 nm) and the red fluorescence of FA3 at λem =675 nm is monitored, we observe evidence for FRET transfer from FA1 to FA3. (F, i) Differential interference contrast (DIC) micrograph of a COP nanoparticle (diameter of ∼500 nm; Fig. 16G). FL, fluorescence. (F, ii) Native autofluorescence of the COP particle under short-wavelength (405 nm) excitation. (F, iii) Fluorescence micrograph of the COP particle after coating with FA4. (F, iv) Combined DIC and fluorescence image of the FA4-coated COP nanoparticle. (Scale bars: 500 nm.)

In addition to binding proteins uniformly to the polymer particles, we provide here clear evidence for quantitative control over the relative composition of the immobilized proteins using two solutions consisting of a mixture of two proteins: cofilin and BSA (6, 7). Both protein solutions were prepared with the same total amount of proteins but with two different relative concentrations: The first solution is 0.1 μg/mL cofilin + 200 μg/mL BSA, whereas the second solution is 10 μg/mL cofilin + 190 μg/mL BSA. We determined that the relative composition of the particle-bound proteins corresponds to that in the

solutions using two methods. First, by dissociating the particle-bound proteins via boiling in a denaturing buffer, we quantify the amount of protein from the two sample populations in two SDS polyacrylamide gels that electrophoretically separate the proteins based on their sizes. One gel was stained to identify BSA and confirmed that the numbers of particles in the two samples were approximately the same (Fig. 17a). The second gel was subjected to Western blotting and confirmed that proportionate amounts of cofilin were retrieved from the particles (Fig. 17b). Second, we monitored the amount of particle-bound cofilin directly by incubation with two FAs: a cofilin-specific FA whose fluorescence strength corresponded to the different amounts of bound cofilin (Fig. 17c) and a nonspecific FA used as a negative control (Fig. 17d). These results thus confirm that the particles can be coated with a controlled amount of a protein that can be retrieved for subsequent characterization and quantification. The particles were acid-washed (in 1 N of HCl for 2 h at 60 °C), pelleted, and washed three times with RIPA buffer [50 mM Tris (pH 7.5), 2 mM EDTA, 150 mM NaCl, 0.1% Nonidet P-40] to remove excess acid.
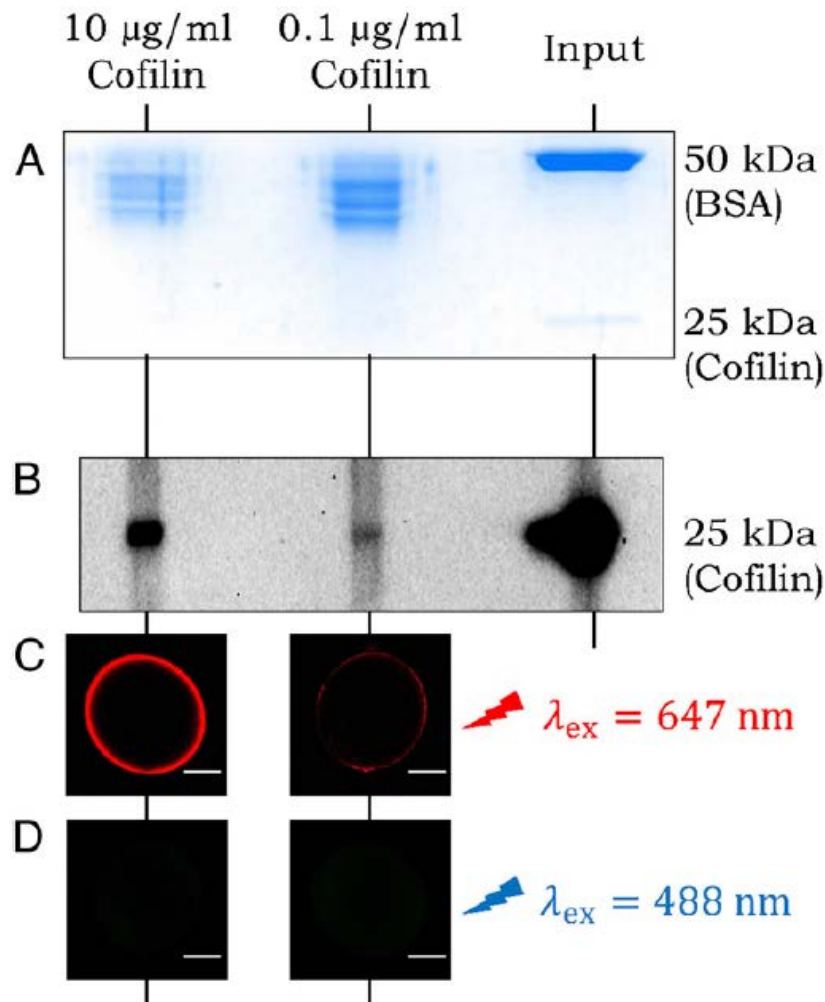
Figure 17. Quantitative assessment of preferential protein coating to polymer particles. (A) Electrophoretic analysis of retrieved protein in a polyacrylamide gel stained for BSA. Lane 3 (Right) shows input BSA and cofilin to confirm their molecular masses (66 kDa and 25 kDa, respectively). Blue polypeptide bands in lanes 1 and 2 show the relative amounts of BSA recovered. No distinct cofilin bands were noted in lanes 1 and 2 because relatively lower amounts of cofilin were loaded in these lanes. (B) Western blot analysis showing higher and lower amounts of cofilin recovered from the particles. There was no detectable degradation of cofilin because a single polypeptide band in each was observed, but some degradation of the recovered BSA is evident by multiple polypeptide bands in the Coomassie-stained gel. BSA has three structural domains that can be easily separated in acidic or alkaline pH, which could explain the appearance of multiple bands in the recovered BSA (6). Red fluorescence is observed from cofilin-specific antibodies, with the fluorescence intensity proportional to the cofilin concentration (C), whereas no (green) fluorescence is observed from nonspecific antibodies (D). (Scale bar: C and D, 10 μm.)

Next, particles were coated with poly-Llysine as described above. The particles were then washed

with RIPA buffer and evenly resuspended in RIPA buffer before equal volumes of particle suspensions

were transferred into two tubes (a and b) and pelleted. The particles in both tubes were then resuspended

and incubated at 4 °C for 12 h with two different protein solutions of cofilin (purified in house) and BSA

31

(Sigma–Aldrich) in RIPA buffer (tube a: 0.1 μg/mL cofilin + 200 μg/mL BSA; tube b: 10 μg/mL cofilin + 190 μg/mL BSA). Subsequently, the particles were centrifuged and washed with RIPA buffer three times. During the last wash, 10% of the particle suspensions from both samples was transferred to a new microcentrifuge tube for staining with antibodies, whereas the remaining 90% of both particle suspensions was transferred to a new microcentrifuge tube containing Laemmli sample buffer and boiled for 5 min to elute the bound proteins. The boiled samples in both tubes a and b were then divided in half and separated on two SDS polyacrylamide gels. The particles were stuck in the wells, but the soluble proteins migrated through the gels. Proteins in one gel were stained with Coomassie Brilliant Blue dye (Sigma–Aldrich), whereas proteins in the other gel were electrophoretically transferred to a PVDF membrane containing protein-binding sites. The membrane was incubated in dry milk solution to block the unoccupied sites and prevent nonspecific binding of antibodies. The membrane was incubated with anticofilin primary antibodies produced in rabbit (Novus Biologicals) and HRP-conjugated anti-rabbit secondary antibodies produced in goat (Jackson ImmunoResearch). Positive signals in the blot were detected using the Immun-Star WesternC Kit (Bio-Rad) and ChemiDoc XRS (Bio-Rad).

The 10% of particles set aside for antibody staining was pelleted and resuspended in RIPA buffer containing 300 ng/mL rabbit anticofilin antibodies and 300 ng/mL mouse anti-α-Tubulin antibodies (Sigma–Aldrich) to confirm saturated binding of the cofilin + BSA mixture to the particles and with 200 μg/mL BSA. The particles were incubated with the antibodies for 12 h at 4 °C before being pelleted and washed three times with RIPA buffer. The particles were then incubated for 4 h at 4 °C in RIPA buffer containing fluorescent secondary antibodies: 500 μg/mL goat anti-mouse–conjugated antibodies Alexa Fluor 488 (Invitrogen) or 500 μg/mL goat anti-rabbit–conjugated antibodies Alexa Fluor 647 (Invitrogen) + 200 μg/mL BSA. The particles were again washed three times in RIPA buffer before being resuspended in glycerol, mounted on slides, and imaged.

Finally, I demonstrate a unique feature of this polymer particle fabrication strategy that highlights its versatility with respect to structural design. By modifying the macroscopic preform structure, I produce a unique particle geometry that enables me to establish microencapsulation of biological materials inside a polymeric shell of the same polymer used in the solid particles used above in the protein-binding experiments. I use collagen as the encapsulant, which may be useful for cosmetics and dental applications[54,55] and serves as a model for other potential biological materials or drugs. Like many biological materials, collagen is a globular solution lacking uniform fluid consistency, and is thus incompatible with fiber drawing and traditional microfluidics-based multiple-emulsion approaches. I obviate this limitation by injecting the desired encapsulant inside a drawn hollow fiber in which a COP layer lines the PSU cladding (Fig. 18a). I inject collagen into the 50-µm-diameter hollow core (Fig. 18c) and thermally induce the PRI, which results in the core breaking up into a necklace of collagen-filled COP microcapsules (Fig. 18d) held stationary in the PSU cladding, which are then released using DMAC (Fig. 18e). I confirm that the microcapsules contain protein by dissolving the COP shell (Fig. 18f) and then using a Coomassie Brilliant Blue dye Bradford protein-binding assay[56] with the recovered cargo.
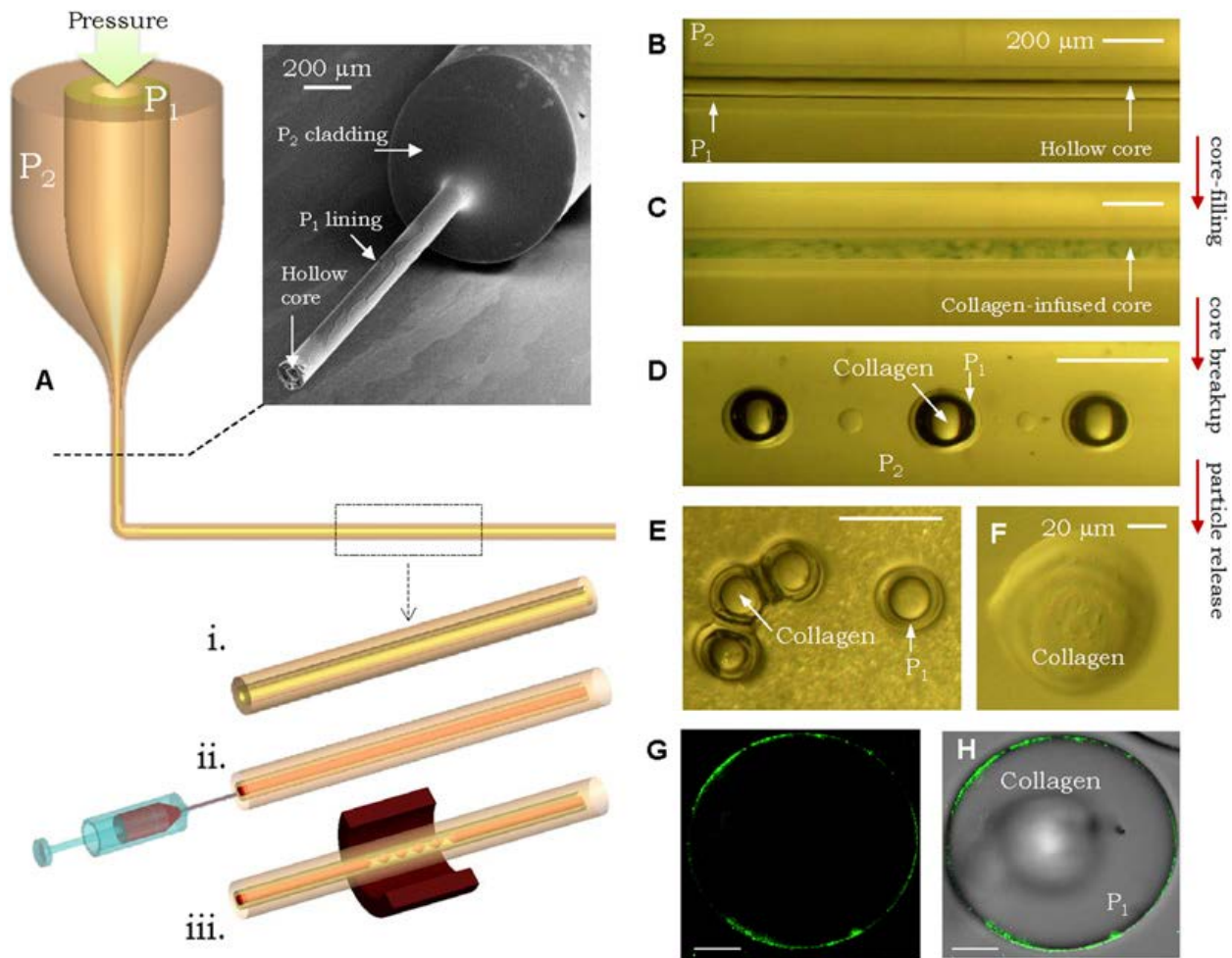
Figure 18. Microencapsulation of biological materials in polymer shells. (A) Schematic of the steps for producing collagen-filled COP microcapsules. (Inset) Hollow-fiber core lined with COP after dissolving the PSU cladding at the fiber tip. Optical transmission micrograph of the side view of the fiber before (B) and after (C) being filled with collagen (slightly doped with a dye for visualization). (D) Encapsulated collagen particles (COP shell) held in the PSU cladding. (E) Collagen/COP microcapsules released from the cladding. (Scale bars: B–E, 200 μm.) (F) Collagen recovered after dissolving the COP shell. (G) A confocal fluorescence micrograph of a collagen-filled microparticle with surface-bound FAs. (H) An overlay of a bright-field confocal micrograph on the fluorescence image from G. (Scale bars: 20 μm.) P1, COP; P2, PSU.

The two modalities discussed thus far, surface functionalization and volume encapsulation, are combined in Fig. 18 g and h, where I demonstrate surface binding of FA4 to collagen-filled COP microcapsules. In comparison to current encapsulation approaches that usually target biodegradable polymeric shells[57,58], my approach enables encapsulation with a wider range of polymers, in addition to access to a broad range of sizes.

CHAPTER 3 MULTIFUNCTIONAL PARTICLES

3.1   Polymer Doping and Extrusion

Functionalized particles have found many uses in both commercial and research applications (REF). Two common functions in commercially available micro- and nano-particles are magnetization and fluorescence. There are companies who indeed produce and make commercially available particles that simultaneously possess both magnetic and fluorescent properties (REF). The need for multifunctional particles, specifically in medicine, has been expressed often and in many places (REF REF REF). Particles designed for drug delivery, for example, would benefit from being able to be guided to the desired location in the body, to be monitored and located through some imaging technique, to safely contain the desired drug to be delivered, and to trigger the release of the drug. There is currently no technique that can easily, efficiently, and repeatedly produce particles that concomitantly possess all of these functionalities. The final stage of my work involving in-fiber particle formation has dealt with the ability to dope polymeric particles with various functionalities and if it is possible to arrange the functionalities in a structured fashion.

The first problem to be addressed was how to add dopants to polymers which could then be extruded into a preform and drawn into fiber. The dopants have to resist the temperatures necessary for extrusion, thermal drawing, and breakup and it must be able to be dispersed into the polymer. Fluorescence is a very common functionality that is added to particles, so it was the first I researched. COP was the polymer of choice, since I had already had a lot of experience working with it and making particles from it, and it is a biocompatible polymer that can be used in biological assays. Organic laser dyes exist that can be made to fluoresce at nearly any visible wavelength, and many are made from materials that can withstand high temperatures. Additionally, their organic nature allows them to be dissolved and dispersed in organic solvents such as chloroform, which can also dissolve COP. The first

laser dye I worked with was DCM dye (Exciton), which fluoresces in the green and red, depending on what wavelength is used as the excitation wavelength. I dissolved 15 grams of COP in 100 mL of chloroform with 15 mg of DCM powder on a magnetic stir plate and allowed the solution to homogenize. The chloroform was evaporated on a hot plate overnight and what remained was placed in a vacuum oven to completely dry out the now-doped COP. What remained was doped COP foam. This foam was then extruded into a 4.5 mm rod which was placed in a 16 mm-diameter polystyrene rod, and this whole preform was drawn into fiber, stacked into a new preform, and drawn down again. Breakup occurred upon thermal treatment of the fiber, and the particles were extracted using DMAC and collected for imaging (Fig. 19). Other organic laser dyes were subsequently tried to show that I can produce particles which fluoresce at any desired wavelength (Fig. 19). Quantum dots were used for fluorescence in the blue and a green fluorescing laser dye from Fabric Holding Inc. were used. Figure 19 shows a three-dimensional confocal fluorescence image of particles inside a polystyrene cladding.
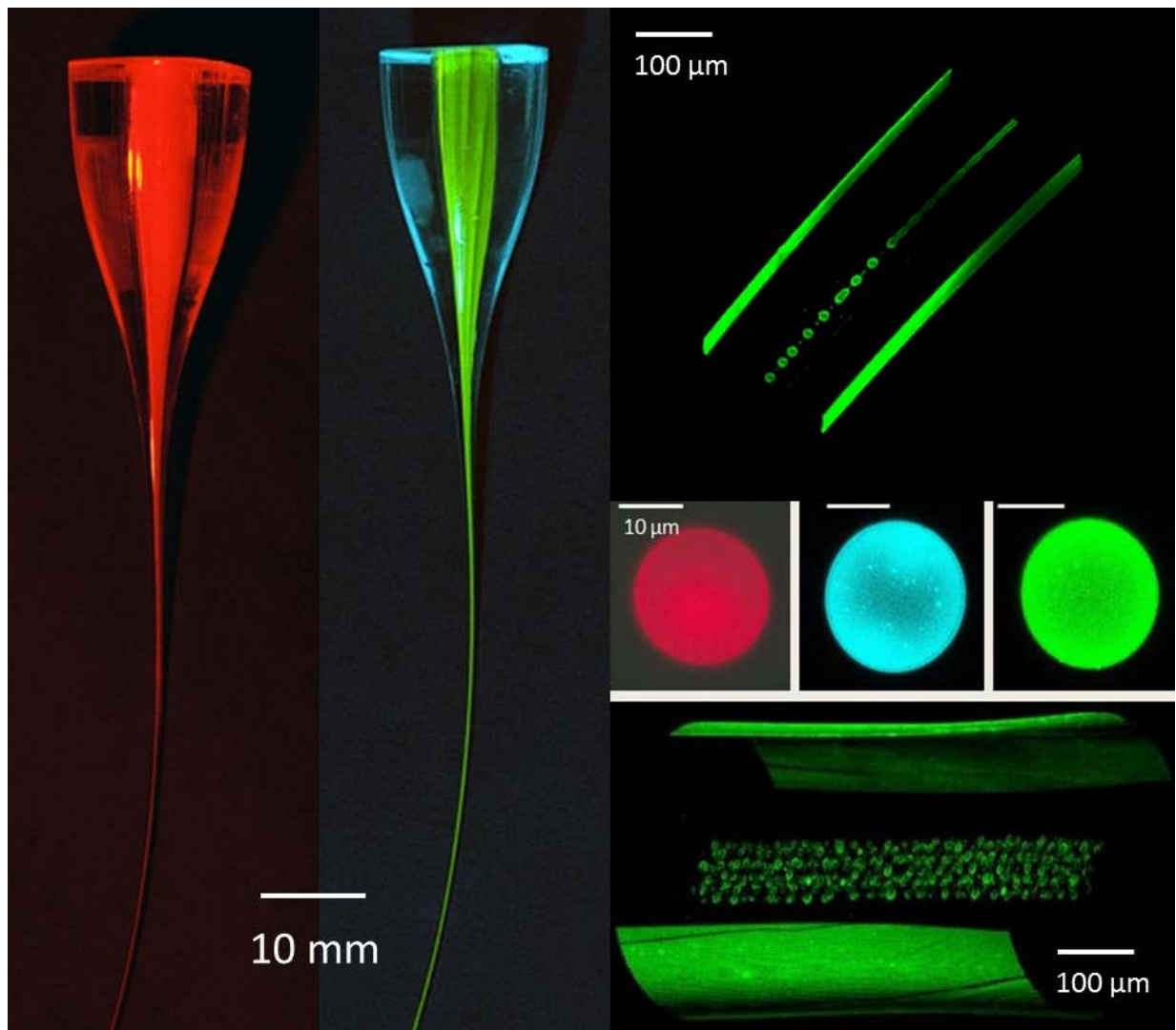
Figure 19. Two photographs of the same preform but under different wavelengths of illumination and through different viewing filters. The laser dye used to dope the COP core can be made to fluorescing in the red if excited in the green or in the green if excited in the blue. To the right are fluorescence images of the fluorescing COP coring breaking up, the particles once removed from the cladding, and the particles still in the cladding.

The next task was to show that the fluorescence could be structured into the particle in the same way I structured the glass particles from Chapter 1. The structures I chose to investigate were core-shell, Janus, one-quarter fluorescing, and two alternating quarters fluorescing at different wavelengths (Fig. 20). The fabrication of the core-shell fluorescing COP microparticles required extruding three polymer

structures followed by the successive thermal drawing of performs into fiber. The three extruded structures were a 5.5-mm-diameter COP rod doped with an organic laser dye, a hollow undoped COP tube, and a 16-mm-diameter polystyrene rod. The dye-doped COP rod was made as follows: first, 15 g of COP pellets were dissolved in chloroform with 0.03 g of FHI laser dye (Fabric Holding Inc.). After stirring for 6 hours, the chloroform was evaporated off, leaving the COP doped with the laser dye. That material was then extruded into a 5.5-mm-diameter rod in a custom-built extrusion machine at 250 C. The undoped COP tube was fabricated as follows: 30 g of COP pellets were used to extrude a 10-mm-diameter hollow rod with an inner diameter of 5 mm. The hollow portion is formed because the die used in this extrusion had a pin placed in the middle so that as material is pushed through the die, the inner portion is blocked, leaving a hollow, cylindrical center. This tube was then machined to make the inner diameter 6 mm. The solid polystyrene rod was extruded with approximately 100 g of polystyrene pellets (Goodfollow Corp.) at 240 C through a 16-mm-diameter die.

With these three extruded structures in hand, the first preform was fabricated as follows: 35-µm-thick sheets of polycarbonate (PC) were rolled around the doped COP rod until the diameter reached 6 mm, and the rod with the PC layer was placed in the hollow, undoped COP tube. This whole structure was then placed in the 16-mm-diameter polystyrene (PS) cladding, in which a 10-mm-diameter hole had been drilled using a lathe. The resulting preform was thermally drawn into a 5-mm-diameter rod in a home-built optical fiber draw tower at 280 C, which was then placed in a second 16-mm-diameter polystyrene rod. This was thermally drawn into a 1-mm-diameter fiber, which was placed in the center of a third 16-mm-diameter polystyrene rod and drawn again into a 1-mm-diameter fiber whose core diameter (the outer, undoped COP layer) was 12 µm. The fiber was thermally treated at 270 C for 5 minutes to induce the PRI and produce spherical particles, which were removed from the cladding by dissolving the polystyrene in dimethylacetamide (DMAC).
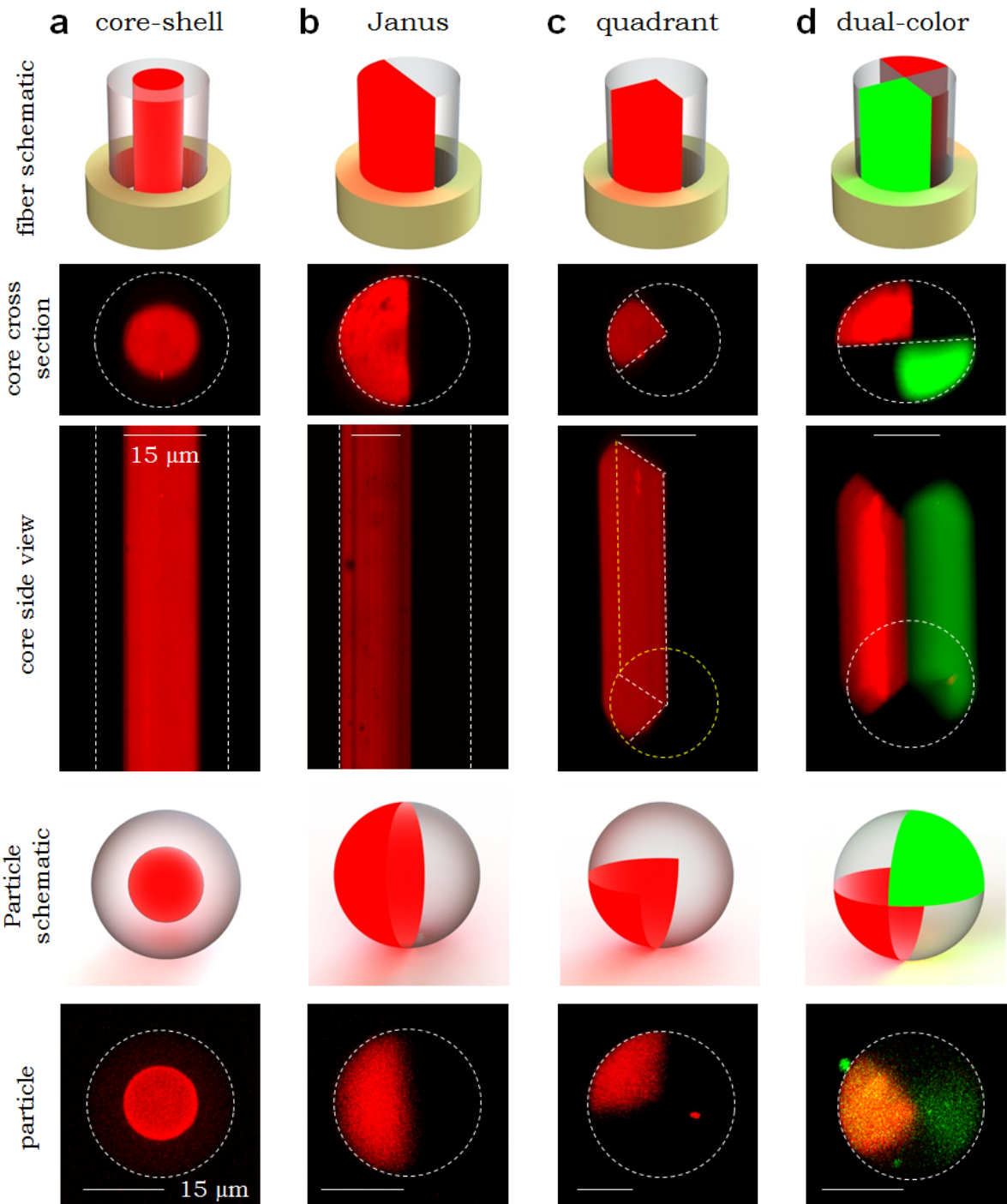
Figure 20. Fiber schematic, fluorescence image of the core cross section, fluorescence image of the side view of the intact fiber core, particle schematic, and fluorescence particle image for the following structures: (a) core-shell, (b) Janus, (c) one-quarter, and (d) dual-color alternating quadrants.

39

The fabrication of the Janus fluorescing particle is again very similar to the above procedures. A section of the 4.5-mm-diameter, FHI laser dye-doped cylindrical COP rod was machined down to a half cylinder. A section of the 4.5-mm-diameter undoped cylindrical COP rod was also machined down to a half cylinder, and the two halves were placed together inside a 16-mm-diameter polystyrene cylindrical rod. This preform was drawn down to a 1-mm-diameter fiber, which was placed in the core of a subsequent 16-mm-diameter polystyrene rod. This second preform was again drawn into a 1-mm-diameter fiber with a core size of 15 µm in diameter. Thermal treatment of this fiber induced the PRI, and the particles were collected by dissolving the polystyrene cladding in DMAC.

The fabrication of the one-quarter fluorescing particle followed very similar steps to the core-shell particle. A section of the 4.5-mm-diameter, FHI laser dye-doped cylindrical COP rod was machined down to a quarter cylinder. A section of the 4.5-mm-diameter undoped COP cylindrical rod was machined into a quarter cylinder, as well as another section that was machined into a half cylinder. The three sections were pieced together to make a cylindrical rod with one quarter of the rod doped with the FHI laser dye, which was placed into a 16-mm-diameter polystyrene cylindrical rod in which a 4.5-mm-diameter hole was drilled on a lathe. The entire preform structure was thus a polystyrene cylinder having a 16 mm diameter and a COP core consisting of the above-mentioned three sections. This preform was drawn down to a 0.9-mm-diameter fiber which was placed in the core of a second 16-mm-diameter polystyrene rod to be drawn down to a second 0.9-mm-diameter fiber. At this stage, the core diameter was approximately 15 µm. The fiber was thermally treated at 270 C for 5 minutes to induce the PRI and produce spherical particles, which were removed from the cladding by dissolving the polystyrene in DMAC. Lastly, the two-quarter two-wavelength fluorescing particle fabrication was the same as the one-quarter except one of the non-fluorescing quarters was swapped for a fluorescing quarter doped with DCM organic laser dye.

3.2 Multi-function Particle Fabrication

In all of the above cases, structuring of a single functionality is shown. Even in the case of two different organic laser dyes in the same particle, the result is still the structuring of the single functionality of fluorescence. The addition of second functionality would result in a truly multi-functional particle. The functionality chosen to demonstrate this was magnetism. Iron oxide nanoparticles are now widely available and can be made to disperse either in an aqueous solution or in an organic solvent solution. Organically dispersible 5 nm-diameter iron oxide particles were purchased from Ocean Nanotech, and came in a chloroform solution. A high doping concentration is needed here because the force generated in the iron oxide nanoparticles must be enough to move the entire COP particle. It would be possible to simply buy a large amount of iron oxide nanoparticles, but a doping concentration of even 1 % would require 150 mg of iron oxide nanoparticles in the typical 15 g COP extrusion done as described in the fluorescing preform extrusions above. Given the high cost of iron oxide nanoparticles ($200 for 50 mg), it would be very difficult to freely experiment if the price of each trial was in the range of thousands of dollars.

To overcome this problem, a small table-top version of an extrusion machine was built that could extrude approximately 1 gram of polymer at a time (Fig. 21). Its operation is essentially identical to that of the large extrusion system, but miniaturized in every aspect with an aperture that produces rods of approximately 2 mm in diameter. A small block of copper with a half-inch diameter chamber is heated by a thermocouple and a turn-crank piston is used to press the material in the chamber.
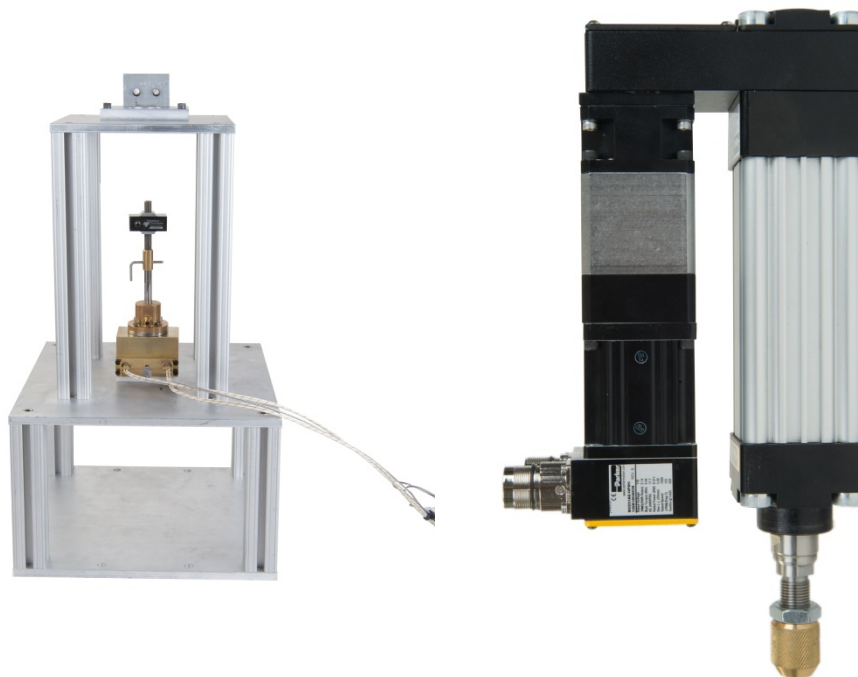
Figure 21. The table-top extrusion system capable of extruding small-diameter rods of approximately 1 gram or less. On the left is the base of the system consisting of a heated chamber where the to-be extruded polymer resides. On the right is the piston motor that compresses the polymer and pushes it through the die at the bottom of the heating chamber.

The doping of the COP with 5 nm-diameter iron oxide nanoparticles was done much in the same way as the doping with organic laser dye, but in different proportions. A beaker with 100 mL of chloroform was placed on a magnetic stirring plate and 2 g of COP were added. The iron oxide nanoparticles came in a 20 mL chloroform solution containing 50 mg of iron oxide. The mass ratio of iron oxide to COP was thus 2.5%. After homogenization, doped COP foam was produced after drying in a vacuum furnace at 100 C for 12 hours. The foam was extruded into a 2.2 mm-diameter rod, which was placed inside an extruded 4.5 mm-diameter COP rod doped with DCM dye after a 2.2 mm-diameter hole was drilled into the DCM-doped rod on a lathe. Polystyrene was again used the cladding, and the

resulting 16 mm-diameter preform was drawn into fiber with an outer diameter of 0.7 mm. The resulting

inner diameter (the DCM-doped portion) was thus 200 µm. A subsequent preform was constructed from

another 16 mm-diameter polystyrene rod, and 25 of the previously drawn fibers were stacked into the

core. After drawing down to an outer diameter of 0.7 mm, resulting in 25 cores each having a diameter of

approximately 8.5 µm. This process was repeated with the end result being a 0.7 mm-diameter fiber with

625 cores each with a diameter of approximately 350 nm.

The emergence of functionalized micro- and nano-particles has led to the development of novel

approaches in the field of biomedical research. Increasing the number of functionalities in these particles

allows for more targeted applications. Surface labeling of nanoparticles can provide enhancement in

particle accumulation in specific tissues and is used to increase the half-life of particle circulation.

Attachment of targeting moieties, like transferrin, can bind to plasma membrane receptors, present in high

concentrations in the target cell type, resulting in endocytosis of the receptor-ligand-particle complex.

Alternatively, the addition of PEG molecules to the surface of particles grants stealth like characteristics

hindering macrophage accumulation. The combination of surface labeling with bespoke particle

structuring has opened the door to application specific particle design, of which has not been

demonstrated. In this study we utilized transferrin, as our targeting molecule, to label our particles.

Confocal microscopy ensured even coating of the fluorescently labeled transferrin on the particle surface

was achieved, and cross sections of the particle reveal the fluorescently doped COP shell along with the

magnetic core (Fig. 22c). The presence of super paramagnetic iron oxide nanoparticles within the core of

these particles allows for the particles to be used in multiple biomedical applications, most notably as a

contrast agent in magnetic resonance imaging (MRI), and in the isolation of circulating tumor cells

(CTCs). Flexibility in particle structuring allows for varying the amount and location of iron oxide

doping. With this method of particle production, scaling particle size up or down is easily achieved. This

can be a valuable advantage in designing particles for biomedical applications, tuneability in drug

delivery and internalization can be achieved by altering particle size. In the case of cell sorting, target cells like circulating tumor cells can be isolated by incubating surface labeled magnetic particles with the cell suspensions or whole blood. Association of the particles with the cells allows for isolation of the specific cell type simply by using a magnet. Within the nanoscale, particles are internalized and accumulate within the cells in a time dependent manner: the more particle accumulation the more sensitive the cells become to the magnetic field (Fig.22e, 22f). Alternatively, larger microscale particles containing a higher mass of super paramagnetic iron oxide nanoparticles can be exploited to reduce cell stress and sorting time. Incubation of surface coated microparticles with target cells does not allow for the internalization of the particle but permits multiple cells to bind to a single particle (Fig 22d). Cells can then be easily dissociated from the particles by acid washing or protease treatment. Finally, the particles can then be recovered by magnetic separation. Increased efficiency of cell separation was achieved through magnetic-activated cell sorting (MACS), resulting in the average isolation of 85% of the cell population (Fig. 22g). Variations in transferrin receptor expression between cells, and the presence of mitotic cells may explain the reduced accumulation of particles in the unsorted 15% of cells. Accumulation within the cells was enriched in transferrin coated particles compared to naïve COP particles or poly-l-lysine coated particles, and resulted in a reduction in the percent of cells isolated 33% and 52% respectively. In contrast, to transferrin, BSA coating prevented particle-cell interactions.
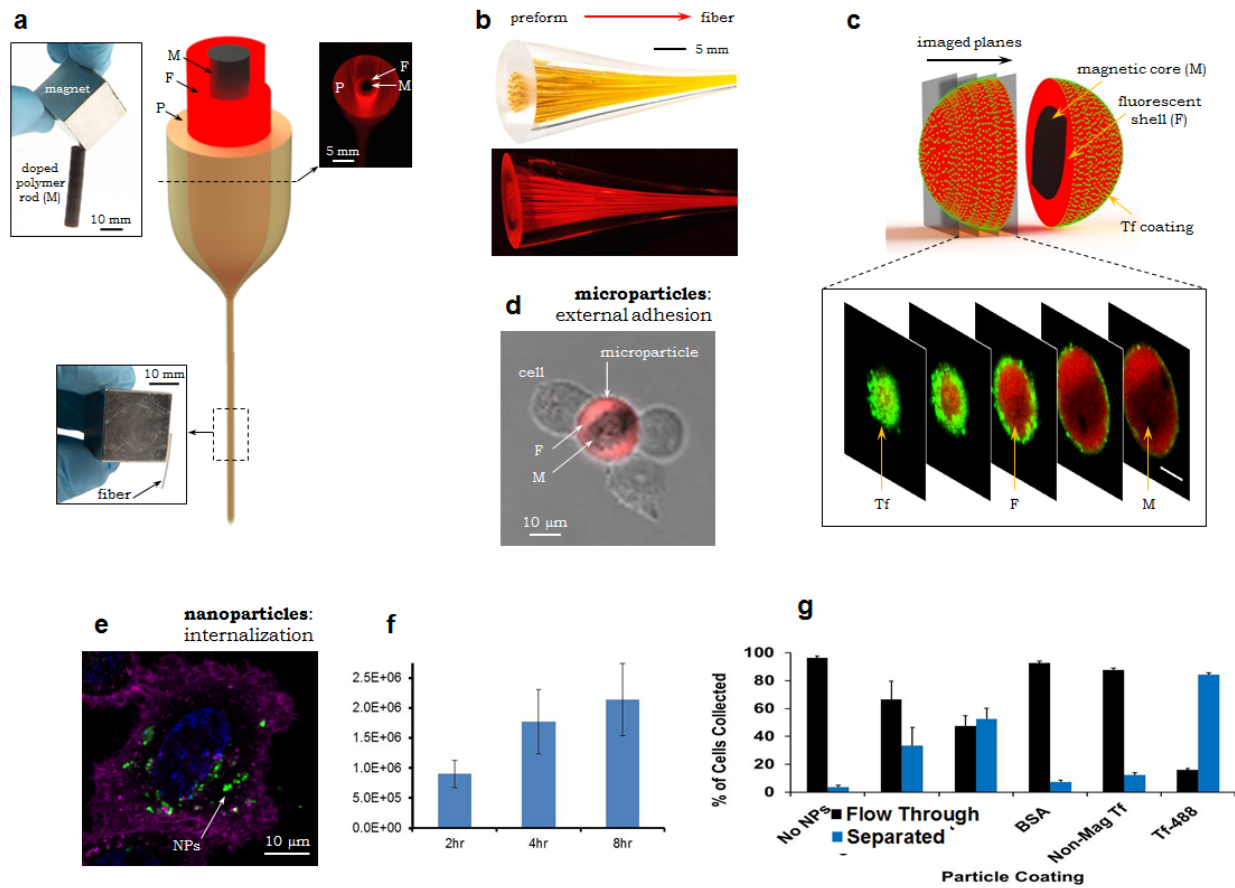
Figure 22. (a) An extruded COP rod doped with iron oxide nanoparticles, a schematic of the preform and fiber structure, a photograph of the preform cross section, and a polystyrene cladding fiber with a magnetically doped COP core hanging from a strong magnet. (b) Photograph of the multi-core preform, both white-light and fluorescing. (c) Schematic and confocal microscopy image of a fluorescent shell/magnetic core particle coating in green-fluorescing transferrin. (d) Micrograph overlay of the bright field and fluorescing images of a fluorescing shell/magnetic core particle with three prostate cancer cells attached. (e) Confocal fluorescence image of a prostate cancer cell with fluorescing shell/magnetic core nanoparticles within the cell membrane. The violet portion is the cell membrane, the blue portion is the cell nucleus, and the green dots are the nanoparticles. (f) Graph representing nanoparticle uptake in cells over time. (g) Graph showing cell recovery using magnetic separation.

The processing of the particles in the above-discussed experiment was as follows: First, particles were isolated from polystyrene cladding by dissolving fibers in DMAC. Particles were separated by applied magnetic field and DMAC was removed. Particles were washed 2x with DMAC to remove residual dissolved cladding. Particles were then washed twice with 2-Propanol to remove excess DMAC and then

three times with phosphate buffered saline (PBS), 0.05% Tween-20. Particles were then resuspended in 250ul diH20.

- 200ul was then transferred to a new to tube and incubated with 0.001% poly-l-lysine in diH20, overnight at 4C while rotating. Next day, particles separated by applied magnetic field and supernatant was removed. Particles were then washed 3x in PBS containing 0.05% Tween-20. Particles were then resuspended in 300ul PBS.

- 150ul of poly-l-lysine coated particles were divided into three tubes and then incubated with or without Transferrin or BSA while rotating at 4deg C overnight.

    1) No protein coating, incubated with PBS only.

    2) Transferrin-488 (1mg/ml) in PBS (Transferrin from human serum, Alexa Fluor® 488 Conjugate)

    3) BSA (1mg/ml) in PBS

Next day, particles separated by applied magnetic field and supernatant was removed. Particles were then washed 3x in PBS containing 0.05% Tween-20. Particles were then resuspended in HAM F-12 media containing 0.5% BSA, 0.1% HI-FBS, 0.1% Pluronic F68

Cell Culture / Particle incubation:

PC-3 cells were grown to ~80% confluence in complete media, HAM F-12 10% HI-FBS. Cells were than serum starved for 3hrs , complete media was removed and replaced with HAM F-12 containing no serum. Following 3 hrs, cells were trypsinized and counted. 50,000 PC-3 cells were transferred to BSA coated microcentrifuge tubes. Equivalent amounts of particle suspensions were then added to all but one tube of cells. Total volumes were brought up to 400ul with HAM F-12 media containing 0.5% BSA, 0.1% HI-FBS, 0.1% Pluronic F68.

1) 50,000 PC-3 cells only (no NPs)

2) 50,000 PC-3 cells + Transferrin coated NPs

3) 50,000 PC-3 cells + BSA coated NPs

4) 50,000 PC-3 cells + Poly-l-lysine coated NPs

5) 50,000 PC-3 cells + Uncoated NPs

Cell-NP suspensions were then incubated at 37 deg C while shaking for 3hrs. Cells associated with NPs were then isolated by applied magnetic field for 20mins. Supernatant containing unbound cells was aspirated and set aside for analysis. Magnetically separated cells were resuspended in PBS containing 0.5% BSA, 0.1% Pluronic F68. Magnetic field was reapplied and supernatant was again aspirated. Cells were then stained in 100ul volume with CellMask Deep Red plasma membrane stain [3ug/ml] for 5 min. 600ul of PBS was then directly added to stained cell suspensions and analyzed immediately by flow cytometry.

3.3 Multi-functional, Multi-material Particle Fabrication

All of the preceding multi-functional particles were made entirely of COP. Finally, I demonstrate the fabrication of multi-functional, multi-material particles. The two structures that I fabricated were: (1) a three layer particle consisting of a magnetically-doped COP core, a middle layer of polystyrene doped with green-fluorescing DCM laser dye, and an outer layer of COP doped with red-fluorescing FHI laser dye and (2) a core-shell structure whose core is magnetically doped polystyrene and whose shell is a Janus structure half of which is doped with DCM and half of which is doped with FHI laser dye.

The fabrication of these preforms was very similar to the all-COP structured fluorescing-core preforms. Multiple doped rods were extruded in the table-top extrusion system. In the case of the three layer particle, three doped rods were extruded: a 2.2-mm-diameter COP rod doped with iron oxide

nanoparticles, a 3.4-mm-diameter polystyrene rod doped with green-fluorescing DCM laser dye, and a 4.5-mm-diameter COP rod doped with red-fluorescing FHI laser dye. A 2.2-mm-diameter hole was drilled into the 3.4-mm-diameter polystyrene rod on a lathe in a machine shop, and a 3.4-mm-diameter hole was drilled into the 4.5-mm-diameter COP rod. The rods appropriately stacked into one another and the stacked structure was placed into a 16-mm-diameter polystyrene rod, which was extruded in the large-scale extrusion system. This was drawn down to a 1-mm-diameter fiber, which was placed into the core of a second 16-mm-diameter polystyrene rod. This second preform was drawn into a 1-mm-diameter fiber, which was then thermally treated at 270 degrees Celsius to induce the PRI. The polystyrene cladding was then dissolved away using DMAC and the particles were collected for imaging.

The fabrication of the fluorescing Janus-shell particle with magnetic core also begin with the extrusion of 3 doped rods: a 2.2-mm-diameter polystyrene rod doped with iron oxide nanoparticles, a 4.5-mm-diameter COP rod doped with green-fluorescing DCM laser dye, and a 4.5-mm-diameter COP rod doped with red-fluorescing FHI laser dye. A 2.2-mm-diameter hole was drilled into both COP rods using a lathe, and then each of them were sanded down into half-cylinders that fit perfectly together to form a whole cylinder. The magnetically doped rod was then placed into the now-whole cylinder comprised of a red-fluorescing and a green-fluorescing half. This whole structure was placed into the core of a 16-mm-diameter polystyrene rod and drawn into a 1-mm-diameter fiber, which was placed into the core of a second 16-mm-diameter polystyrene rod. This second preform was drawn into a 1-mm-diameter fiber, which was then thermally treated at 270 degrees Celsius to induce the PRI. The polystyrene cladding was then dissolved away using DMAC and the particles were collected for imaging.
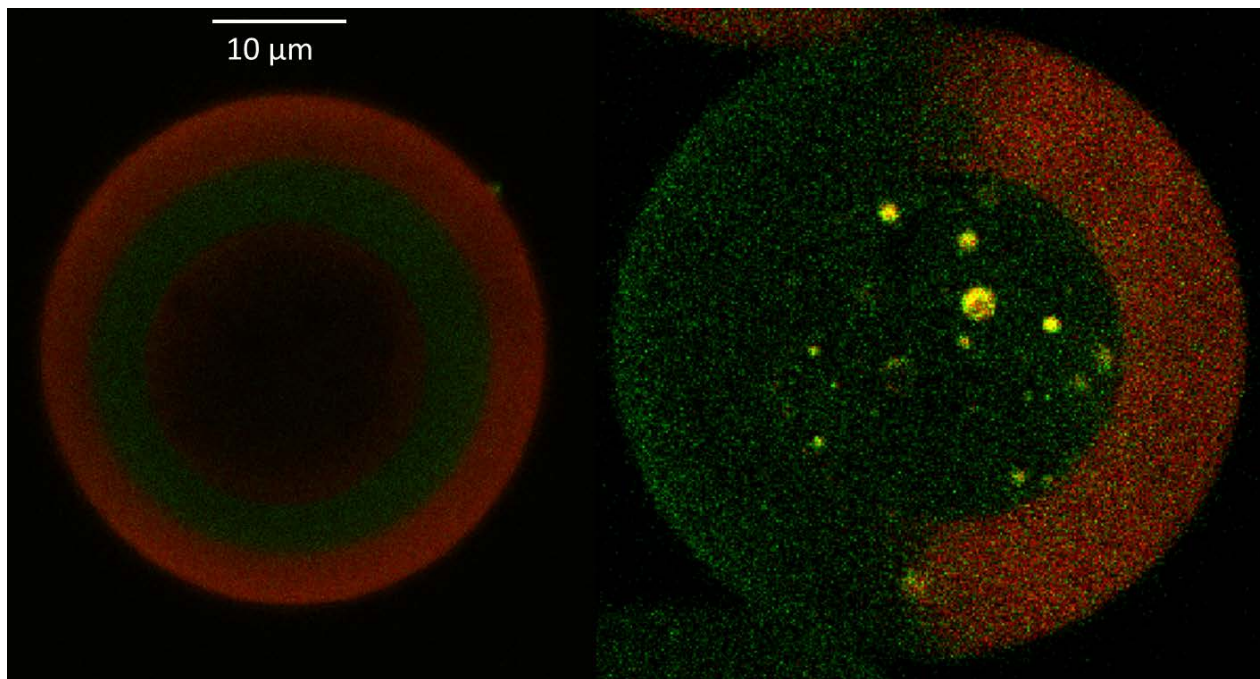
Figure 23. (left) 3-layer particle consisting of a magnetically doped COP core, a DCM doped middle layer of polystyrene, and a FHI doped outer layer of COP. (right) Janus-fluorescing-shell with a magnetic core consisting of a magnetically doped polystyrene core and an outer layer that is made of a half-spherical shell of DCM-doped COP and a half-spherical shell of FHI-doped COP.

The fact that the core, the magnetically-doped polystyrene, also appears to be fluorescing in the green could be due to one of two things: auto fluorescence which can result from exciting polystyrene in the blue region of the spectrum, or diffusion of the FHI dye from the COP layer into the lower viscosity polystyrene during thermal treatment to induce the PRI. Further research is required to discern which of these hypotheses is correct.

CHAPTER 4 CONCLUSION

During my research, I have demonstrated that the spherical droplet formation of one material in another through an in-fiber Plateau-Rayleigh Capillary Instability (PRI) is a robust, flexible, nearly scale-invariant, and scalable method that may be used for the efficient production of multi-functional, multi-material particles. The PRI allows for the formation of particles from low-temperature glasses, polymers, and biological materials (such as collagen). The ability to employ a stack-and-draw process of placing a large number of fibers into the core of a preform enables the parallelization of the PRI in a single fiber, increasing the particle yield. The construction of the preform at the centimeter scale makes possible complex structuring of the core to be drawn in the cladding material. The resulting particle inherits the structure of the core of the fiber, and complex structures such as Janus, beach-ball, and multilayer spheres. Furthermore, through the common-solvent doping and extrusion of polymers, functionalities may be introduced such as fluorescence and magnetic properties.

4.1 Future Work

In addition to addressing many of the challenges involved in particle fabrication, this work also opens up new possibilities for exploration of this fluid dynamical phenomenon. One of these questions involves the optical properties of multi-material, multi-layer particles and the scattering induced from these structures. Another involves the possibility of generating particles mode from biodegradable polymers, opening up the potential for applications in drug doping and drug delivery. For drug delivery applications, materials that break down *in vivo* and that have been shown to be safe *in vivo* would be desirable. To this end, initial work has been conducted in the extrusion and thermal drawing of multi-

material fibers made from biodegradable polymers such as polyethylene glycol (PEG), polycaprolactone (PCL), and polylactic-co-glycolic acid (PLGA).
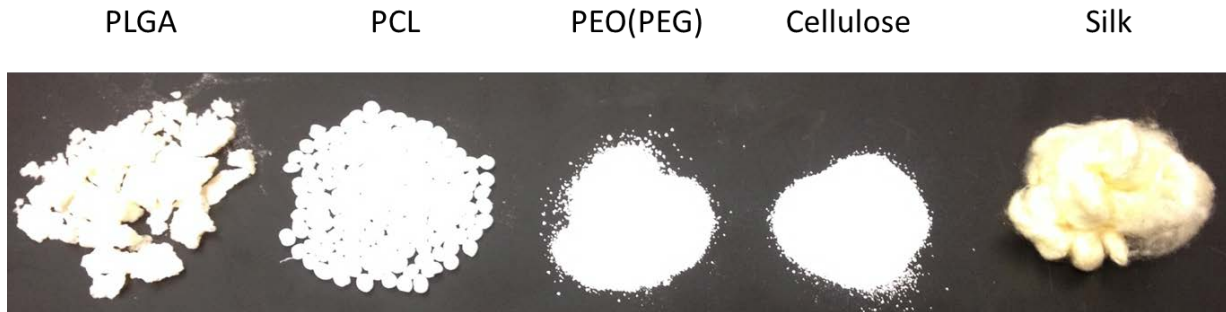
Figure 24. Examples of 5 different biodegradable polymers.

Care needs to be taken when processing these polymers. They typically have a relatively low softening-temperature (below 100 ° C). In our conventional fiber draw tower, the thermal gradient is very gradual, causing the entire preform to soften and begin to draw all at once. To get around this, a simple ring-heater in ambient environment has been employed to heat preforms made from these materials, and they may be drawn by hand in this setup. In this way, fibers have been drawn with a polyethylene oxide (the higher molecular weight version of PEG) cladding and a PLGA cladding. Furthermore, by dissolving PLGA in a mixture of methanol and chloroform, it was possible to dope the PLGA with minocycline, a common antibiotic (Fig. 25).
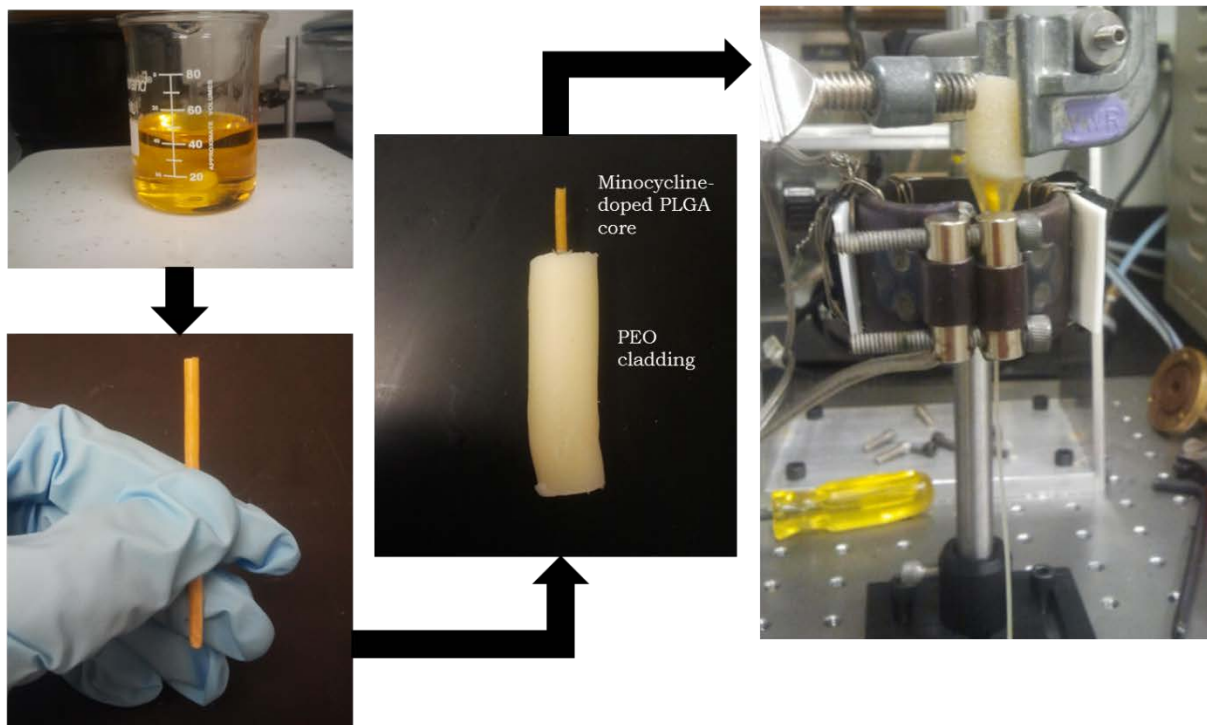
Figure 25. The process of doping PLGA biodegradable polymer with the antibiotic minocycline, extruding the doped PLGA, and the drawing of the PLGA in a cladding of PEO into a fiber using a ring-heater setup.

With these fibers in hand, thermal treatment has been attempted to induce the PRI, with preliminary results showing that particle formation is possible. So far, the results have been inconsistent, but some spherical particles have been retrieved after the dissolution of the PEO cladding. Because of the low viscosity of these materials (Fig. 26) surface tension is decreased compared to that of COP, and I believe that this is further exacerbated by the lower surface energy between PLGA and PEO, which would also decrease the surface tension and make particle formation more difficult.

COP Viscosity Curve

PEO Viscosity Curve
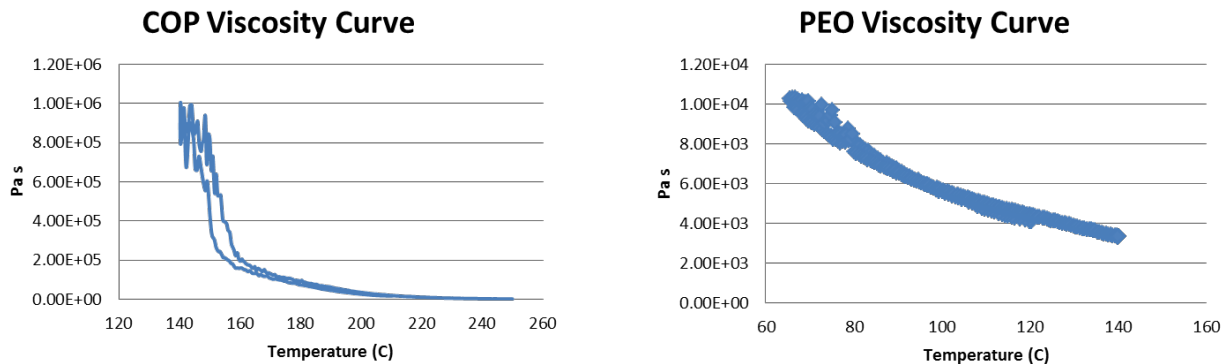
Figure 26. Comparison of the viscosity vs. temperature curves of COP and PEO

Nonetheless, initial results indicate that particle formation is at least possible, and the efficiency

and repeatability of this process may be increased by engineering a better heating setup for the preform

during drawing and the more accurate observation of tension during fiber drawing: as fiber tension

increases during drawing, so does surface tension once the materials are thermally treated, as the tension

built into the polymers during drawing are released once the materials soften upon thermal treatment. One

of the properties of biodegradable polymers is that they typical are susceptible to dissolution in most

organic solvents. Therefore, finding an appropriate solvent that will dissolve the cladding material

without harming the core particle material might appear to be difficult. However, due to the availability of

polymers such as PEO that dissolve in water, this problem begins to evaporate. My preliminary results in

this endeavor reveal that it is possible to remove PLGA particles from a PEO cladding by dissolving the

PEO in water and cladding the particles after centrifugation and resuspension an aqueous solution (Fig.

27). It can be seen that the particles resulting from the in-fiber PRI of PLGA in PEO that the particles are

not perfectly spherical, as was seen in the chalcogenide glass particles and the COP particles previously.

This can be most likely attributed to the low viscosity and/or low surface tension between the PLGA and

PEO which would decrease the surface tension that causes the PLGA to ball up from a previously

cylindrical state. Experiments will be conducted in the future to measure the surface tension of PGLA on

a PEO substrate, which will allow me to discern what the cause for the poor particle generation.
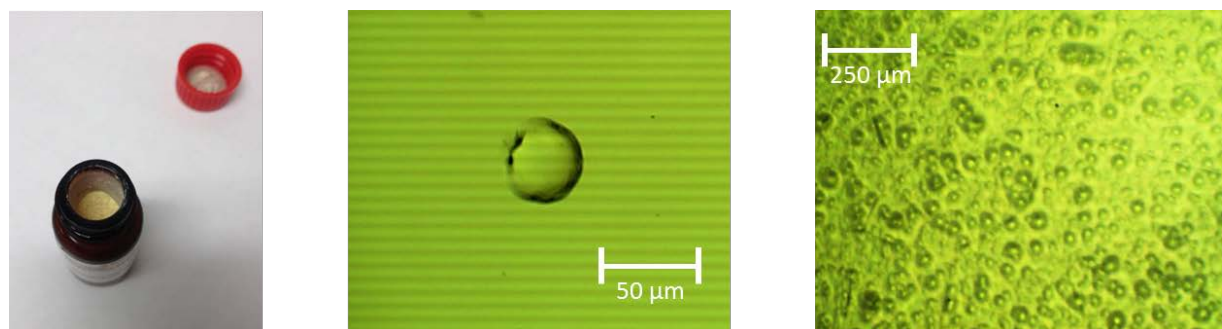
Figure 27. (left to right) Minocycline powder as purchased from the supplier, a single PLGA particle doped with minocycline, and a group of PLGA particles after being released from the PEO cladding by dissolving in water.

Lastly, experiments were conducted to investigate whether the minocycline that was incorporated

into the PLGA particles was still active and able to inhibit bacterial growth and what the release rate of

the minocycline was into solution. One concern I had initially was the whether the minocycline would

degrade during the thermal treatment used to induce the PRI. Thus, the resulting particles were placed in a

culture of *e. coli* and allowed to incubate, and the resulting solution was monitored to see if the *e.coli*

growth was inhibited or not. This was quantified by taking a small volume of the solution and measuring

the absorption at 600 nm: the higher the absorption, the more *e. coli* there is in the solution. Different

samples were used: a control containing only *e. coli* in solution, a sample containing only PLGA with no

minocycline, a sample of PLGA particles doped with 1% minocycline, and a sample of PLGA particles

doped with 5% minocycline. The 1% and 5% samples were then taken and diluted at various amounts and

compared to one another. The performance of these samples was then compared to different minocycline

standards: solutions where minocycline was added directly to the *e. coli* solutions.
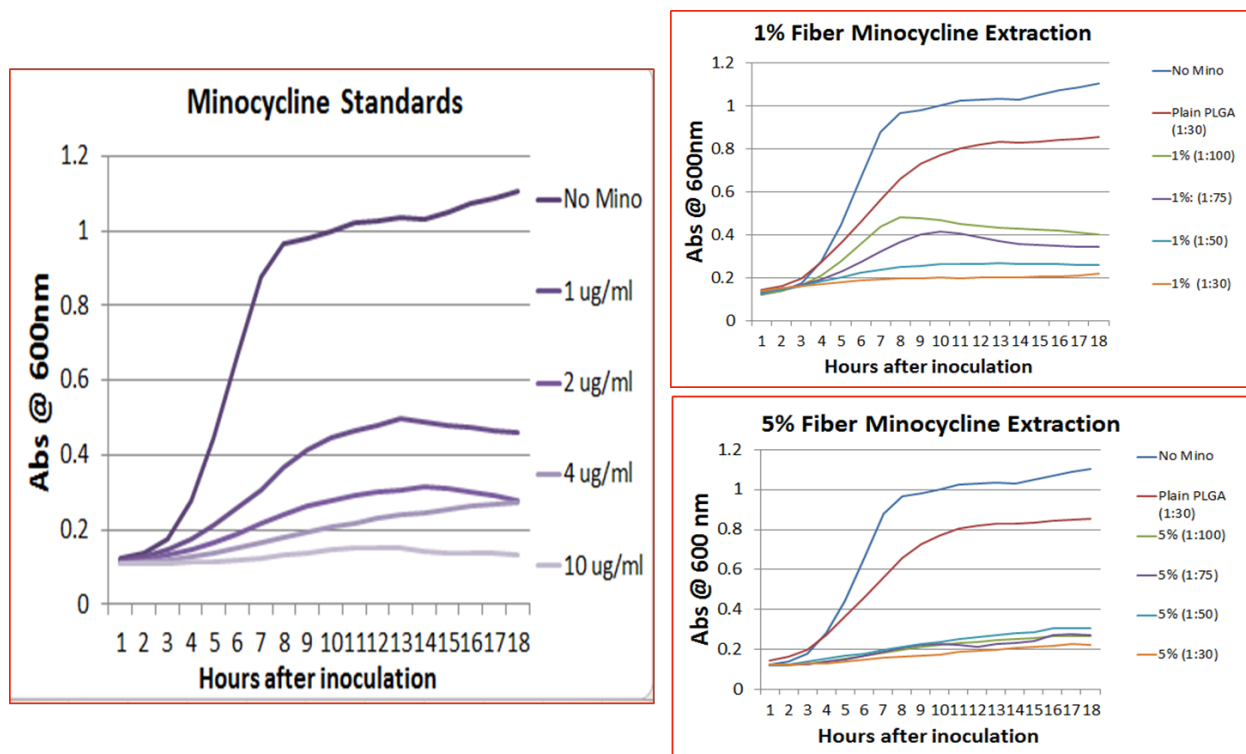
Figure 28. Absorption of solutions containing e. coli and minocycline or PLGA-doped minocycline particles. On the left is a graph showing the inhibition of e. coli growth in solution when various concentrations of minocycline are added. To the right are two graphs showing the same data for PLGA particles doped with 1% and 5% minocycline. The higher concentrations of minocycline inhibit the growth of e. coli, lowering the absorption at 600 nm.

These preliminary results show that the in-fiber PRI can be used to produce particles from biodegradable polymers, and these polymers can be doped with antibiotics that are still active after particle formation. Given that I showed earlier the fabrication of multi-layer particles, it is conceivable that multi-layer biodegradable particles can be made where each layer is doped differently and may consist of different materials. Thus, it may be possible to tailor the release profile of the drug or drugs for whatever application is desired. In addition, if functionalities can be added in addition to drugs, particles can be made that can be monitored, moved around using a magnetic field, attach to a specific surface or sell, and release the drug on command. Furthermore, if thermal treatment is not used to induce the PRI,

the fibers themselves may be very useful as sutures or stitches that can be used to decrease the possibility of infection occurring after surgery, for example.

REFERENCES

1. Timko, B. P. et al. Advances in drug delivery. *Annu. Rev. Mater. Res*. **41**, 1–20 (2011).

2. Wang, J., Byrne, J.D., Napier, M. E. & DeSimone, J. M. More effective nanomedicines through particle design. *Small* **7**, 1919–1931 (2011).

3. Bell, A. T. The impact of nanoscience on heterogeneous catalysis. *Science* **299**, 1688–1691 (2003).

4. Souto, E. B. & Muller, R. H. Cosmetic features and applications of lipid nanoparticles. *Int. J. Cosmet. Sci.* **30**, 157–165 (2008).

5. Rotello, V. Nanoparticles: Building Blocks for Nanotechnology (Springer, 2003).

6. Cao, G. Nanostructures and Nanomaterials: Synthesis, Properties and Applications (Imperial College Press, 2004).

7. Vollath, D. Nanomaterials: An Introduction to Synthesis, Properties and Application (Wiley-VCH, 2008).

8. Merkel, T. J. et al. Scalable shape-specific, top-down fabrication methods for the synthesis of engineered colloidal microparticles. *Langmuir* **26**, 13086–13096 (2010).

9. Utada, A. S. et al. Monodisperse double emulsions generated from a microcapillary device. *Science* **308**, 537–541 (2005).

10. Dendukuri, D. & Doyle, P. S. The synthesis and assembly of polymeric microparticles using microfluidics. *Adv. Mater.* **21**, 4071–4086 (2009).

11. Dendukuri, D., Pregibon, D.C., Collins, J., Hatton, T. A.& Doyle, P.S. Continuous-flow lithography for high-throughput microparticle synthesis. *Nature Mater.* **5**, 365–369 (2006).

12. Hernandez, C. J. & Mason, T.G. Colloidal alphabet soup: Monodisperse dispersions of shape-designed LithoParticles. *J. Phys. Chem. C* **111**, 4477–4480 (2007).

13. Rolland, J. P. et al. Direct fabrication and harvesting of monodisperse, shape specific nano-biomaterials. *J. Am. Chem. Soc.* **127**, 10096–10100 (2005).

14. Derveaux, S., et al. Synergism between particle-based multiplexing and microfluidics technologies may bring diagnostics closer to the patient. *Anal Bioanal Chem* **391**, 2453–2467 (2008).

15. Wu, J., et al. Motion-based DNA detection using catalytic nanomotors. *Nat Commun*, 10.1038/ncomms1035 (2010).

16. Zhang, Y., et al. Synthesis, biodistribution, and microsingle photon emission computed tomography (SPECT) imaging study of technetium-99m labeled PEGylated dendrimer poly(amidoamine) (PAMAM)-folic acid conjugates. *J Med Chem* **53**, 3262–3272 (2010).

17. Bhavsar, M.D., Amiji, M.M. Polymeric nano- and microparticle technologies for oral gene delivery. *Expert Opin Drug Deliv* **4**, 197–213 (2007).

18. Champion, J.A., Katare, Y.K., Mitragotri, S. Particle shape: A new design parameter for micro- and nanoscale drug delivery carriers. *J Control Release* **121**, 3–9 (2007).

19. Singh, R., Lillard, J.W., Jr. Nanoparticle-based targeted drug delivery. *Exp Mol Pathol* **86**, 215–223 (2009).

20. El Kaoutit, M., Naggar, A.H., Naranjo-Rodríguez, I., de Cisneros, J.L. Graphite grains studded with silver nanoparticles: description and application in promoting direct biocatalysis between heme protein and the resulting carbon paste electrode. *Colloids Surf B Biointerfaces* **92**, 42–49 (2012).

21. Bai. M.-Y., et al. A facile and general method for the encapsulation of different types of imaging contrast agents within micrometer-sized polymer beads. *Adv Funct Mater* **22**, 764–770 (2012).

22. Sheng, Y., et al. Long-circulating polymeric nanoparticles bearing a combinatorial coating of PEG and water-soluble chitosan. *Biomaterials* **30**, 2340–2348 (2009).

23. Tsai, M.J., et al. Baicalein loaded in tocol nanostructured lipid carriers (tocol NLCs) for enhanced stability and brain targeting. *International Journal of Pharmaceutics* **423**, 461–470 (2012).

24. Haley, B., Frenkel, E. Nanoparticles for drug delivery in cancer treatment. *Urol Oncol* **26**, 57–64 (2008).

25. Farokhzad, O.C., et al. Targeted nanoparticle-aptamer bioconjugates for cancer chemotherapy in vivo. *Proc Natl Acad Sci USA* **103**, 6315–6320 (2006).

26. Chen, H., et al. Preparation and characterization of PE38KDEL-loaded anti-HER2 nanoparticles for targeted cancer therapy. *J Control Release* **128**, 209–216 (2008).

27. Greenhalgh, K., Turos, E. In vivo studies of polyacrylate nanoparticle emulsions for topical and systemic applications. *Nanomedicine* **5**, 46–54 (2009).

28. Hu, C.M., Fang, R.H., Copp, J., Luk, B.T., Zhang, L. A biomimetic nanosponge that absorbs pore-forming toxins. *Nat Nanotechnol.* **8**, 336–340 (2013).

29. Yeste, A., Nadeau, M., Burns, E.J., Weiner, H.L., Quintana, F.J. Nanoparticle-mediated codelivery of myelin antigen and a tolerogenic small molecule suppresses experimental autoimmune encephalomyelitis. *Proc Natl Acad Sci USA* **109**, 11270–11275 (2012).

30. Li, T. (ed.) Optical Fiber Communications Vol. 1, Fiber Fabrication (Academic, 1985).

31. Eggers, J. & Villermaux, E. Physics of liquid jets. *Rep. Prog. Phys.* **71**, 036601 (2008).

32. Abouraddy, A. F. et al. Towards multimaterial multifunctional fibers that see, hear, sense and communicate. *Nature Mater.* **6**, 336–347 (2007).

33. Shabahang, S., Kaufman, J. J., Deng, D. S. & Abouraddy, A. F. Observation of the Plateau-Rayleigh capillary instability in multi-material optical fibers. *Appl. Phys. Lett.* **99**, 161909 (2011).

34. Sjoblom, J. Encyclopedic Handbook of Emulsion Technology (Marcel Dekker, 2001).

35. Walther, A. & Muller, A. H. E. Janus particles. *Soft Matter* **4**, 663–668 (2008).

36. Kaufman, J. J. et al. Thermal drawing of high-density macroscopic arrays of well-ordered sub-5-nm-diameter nanowires. *Nano Lett.* **11**, 4768–4773 (2011).

37. Nie, Z. H. et al. Emulsification in a microfluidic flow-focusing device: Effect of the viscosities of the liquids. *Microfluidics and Nanofluidics* **5**, 585–594 (2008).

38. Tomotika, S. On the instability of a cylindrical thread of a viscous liquid surrounded by another viscous fluid. *Proc. R. Soc. Lond. A* **150**, 322–337 (1935).

39. Deng, D. S. et al. In-fiber nanoscale semiconductor filament arrays. *Nano Lett.* **8**, 4265–4269 (2008).

40. Nisisako, T. & Torii, T. Microfluidic large-scale integration on a chip for mass production of monodisperse droplets and particles. *Lab Chip* **8**, 287–293 (2008).

41. Smith, K. A., Solis, F. J. & Chopp, D. L. A projection method for motion of triple junctions by levels sets. *Interfaces Free Bound.* **4**, 263–276 (2002).

42. Dussan, V. E. B. On the spreading of liquids on solid surfaces: static and dynamic contact lines. *Annu. Rev. Fluid Mech.* **11**, 371–400 (1979).

43. de Gennes, P. G. Wetting: statics and dynamics. *Rev. Mod. Phys.* **57**, 827–863 (1985).

44. Israelachvili, J. N. Intermolecular and Surface Forces (Academic, 1992).

45. Nunes, P.S., Ohlsson, P.D., Ordeig, O., Kutter, J.P. Cyclic olefin polymers: Emerging materials for lab-on-a-chip applications. *Microfluid Nanofluid* **9**, 145–161 (2010).

46. Kai, J., Sohn, Y.S., Ahn, C.H. Proceedings of uTAS 2003–Seventh International Conference on Miniaturized Chemical and Biochemical Analysis Systems, eds Northrup MA, Jensen KF, Harrison DJ (Transducers Research Foundation, Squaw Valley, CA), pp 1101–1104 (2003).

47. Jena, R.K., Yue, C.Y. Cyclic olefin copolymer based microfluidic devices for biochip applications: Ultraviolet surface grafting using 2-methacryloyloxyethyl phosphorylcholine. *Biomicrofluidics* **6**, 12822–1282212 (2012).

48. Tao, G., Shabahang, S., Banaei, E.-H., Kaufman, J.J., Abouraddy, A.F. Multimaterial preform coextrusion for robust chalcogenide optical fibers and tapers. *Opt Lett* **37**, 2751–2753 (2012).

49. Chen, K.Y., et al. Asymmetric chitosan membrane containing collagen I nanospheres for skin tissue engineering. *Biomacromolecules* **10**, 1642–1649 (2009).

50. Sakai, K., Hashimoto, Y., Baba, S., Nishiura, A., Matsumoto, N. Effects on bone regeneration when collagen model polypeptides are combined with various sizes of alpha-tricalcium phosphate particles. *Dent Mater J* **30**, 913–922 (2011).

51. Alarcon, E.I., et al. The biocompatibility and antibacterial properties of collagen-stabilized, photochemically prepared silver nanoparticles. *Biomaterials* **33**, 4947–4956 (2012).

52. Lippincott-Schwartz, J., Snapp, E., Kenworthy, A.K. Studying protein dynamics in living cells. *Nat Rev Mol Cell Biol* **2**, 444–456 (2001).

53. Volkhard, H. Principles of Computational Cell Biology (Wiley–VCH, Weinheim, Germany 2008).

54. Helary, C., et al. Concentrated collagen hydrogels as dermal substitutes. *Biomaterials* **31**, 481–490 (2010).

55. Thoma, D.S., Sancho-Puchades, M., Ettlin, D.A., Hämmerle, C.H., Jung, R.E. Impact of a collagen matrix on early healing, aesthetics and patient morbidity in oral mucosal wounds—A randomized study in humans. *J Clin Periodontol* **39**, 157–165 (2012).

56. Bradford, M.M. A rapid and sensitive method for the quantitation of microgram quantities of protein utilizing the principle of protein-dye binding. *Anal Biochem* **72**, 248–254 (1976).

57. Imoto, T., Kida, T., Matsusaki, M., Akashi, M. Preparation and unique pH-responsive properties of novel biodegradable nanocapsules composed of poly(gamma-glutamic acid) and chitosan as weak polyelectrolytes. *Macromol Biosci* **10**, 271–277 (2010).

58. Hudson, D., Margaritis, A. Biopolymer nanoparticle production for controlled release of biopharmaceuticals. *Crit Rev Biotechnol*, 10.3109/07388551.2012.743503 (2013).

59. Kircher, M.F., et. al. A brain tumor molecular imaging strategy using a new triple-modality MRI-photoacoustic-Raman nanoparticle. *Nature Medicine* **18**, 829-834 (2012).